RESEARCH ARTICLE
10.1029/2019JD030544

Key Points:
- Efficient ozone production is driven by availability of local NOx and highly reactive VOCs and continues during the transport into mountains
- Key species driving ozone production include CO, formaldehyde, higher alkanes, acetaldehyde, and isoprene
- Most of formaldehyde and acetaldehyde is chemically produced and due to methane oxidation and emissions of higher alkanes, isoprene, and ethane

Supporting Information:
- Supporting Information S1

Correspondence to:
G. Pfister,
pfister@ucar.edu

Citation:
Pfister, G., Wang, C.-T., Barth, M., Flocke, F., Vizuete, W., & Walters, S. (2019). Chemical characteristics and ozone production in the Northern Colorado Front Range. *Journal of Geophysical Research: Atmospheres*, *124*, 13,397–13,419. https://doi.org/10.1029/2019JD030544

Received 26 FEB 2019
Accepted 8 NOV 2019
Accepted article online 13 NOV 2019
Published online 3 DEC 2019

Chemical Characteristics and Ozone Production in the Northern Colorado Front Range

Gabriele Pfister[1], Chi-Tsan Wang[2], Mary Barth[1], Frank Flocke[1], William Vizuete[2], and Stacy Walters[1]

[1]National Center for Atmospheric Research, Atmospheric Chemistry Observations and Modeling Laboratory, Boulder, CO, USA, [2]Department of Environmental Sciences and Engineering, University of North Carolina, Chapel Hill, NC, USA

Abstract We use the extensive set of aircraft and ground-based observations from the NSF/National Center for Atmospheric Research (NCAR) and State of Colorado Front Range Air Pollution and Photochemistry Éxperiment and the NASA DISCOVER-AQ experiments in summer 2014 together with the regional chemical transport model Weather Research and Forecast Model with Chemistry (WRF-Chem) to study the ozone production and chemical regimes in the Northern Colorado Front Range (NFR). We apply the model's Integrated Reaction Rate capability and chemical tendencies diagnostics and present results from an in-depth analysis of the ozone formation in various NFR regions for a case study of 12 August 2014. We further apply these diagnostics along a WRF online trajectory to assess the chemical evolution of an airmass during transport. The results show efficient ozone production within the NFR driven by the availability of NO_x and an abundance of highly reactive volatile organic compound and also continued ozone production during the transport into the mountains. We identify CO, formaldehyde, higher alkanes, acetaldehyde, and isoprene among the volatile organic compound species with the highest efficiency in ozone production. Formaldehyde and acetaldehyde concentrations in the NFR have a significant contribution from photochemical production, which in turn is linked back to methane oxidation and to emissions of higher alkanes, isoprene, ethane, and propane. This study provides valuable policy information into the chemical fingerprint of surface ozone in the NFR, an area that is in nonattainment of the U.S. EPA ozone health standards and demonstrates the capability of the newly added diagnostic tool in WRF-Chem to address the drivers behind secondary production of pollutants in greater detail.

Plain Language Summary The Colorado Northern Front Range (NFR) frequently exceeds national health standards for ozone. Understanding the reasons behind these trends and how they relate to local emissions is crucial for developing control strategies. Using measurements from two major field campaigns in summer 2014 together with chemical transport modeling, we show that ozone is produced efficiently within the NFR driven by availability of local NO_x and an abundance of highly reactive volatile organic compounds (VOCs). On high ozone days, upslope flows are frequent and ozone continues to be produced during transport of air from the NFR into the mountains with ozone values in the pristine areas sometimes exceeding NFR values.

Chemical analysis shows that key VOCs include carbon monoxide, formaldehyde, higher alkanes, acetaldehyde, and isoprene. Higher alkanes and isoprene are related to direct emissions from oil and natural gas activities and to direct emissions from biogenic sources, respectively. A small part of ambient concentrations of formaldehyde and acetaldehyde is related to direct emissions, but the dominant part is produced photochemically from methane oxidation and emissions of higher alkanes, isoprene, ethane, and propane. Knowledge about the role of different VOC precursors provides valuable information to policy makers and helps develop efficient and cost-effective control strategies.

1. Introduction

The Colorado Northern Front Range (NFR) Metropolitan Area including Denver and surrounding areas houses approximately 4.8 million people and since 2007 has been classified by the U.S. EPA as a nonattainment area for ozone (O_3) due to its summertime exceedances of the National Ambient Air Quality Standard of 75 ppb for ozone. As of summer 2018, the NFR did not appear to be able to meet this standard which likely will elevate the area to a “serious” classification for an ozone nonattainment area. In 2015, the EPA lowered

the National Ambient Air Quality Standard to 70 ppb which will be in effect in the near future and is likely to be exceeded by the NFR (Colorado Department of Public Health and Environment, 2016).

Ozone near the surface is a harmful pollutant with negative effects on human health and the environment. It is produced photochemically from the oxidation of volatile organic compounds (VOCs), which produces hydroperoxy (HO_2) and organic peroxy (RO_2) radicals. These peroxy radicals react with nitrogen oxide (NO) to form nitrogen dioxide (NO_2), which then is photolyzed to form new ozone (Chameides et al., 1992). This process is driven by solar radiation and is therefore typically strongest during midday and in summertime. Ozone production is strongly influenced by the availability of NO_x and VOCs both originating from a vast variety of natural and anthropogenic sources and is also highly dependent on the reactivity of individual compounds as part of the VOC mixture.

Compared to the eastern United States, where ozone levels have declined over the last two decades (Cooper et al., 2014; Simon et al., 2015), summertime ozone in the NFR and similarly in other regions of the western United States has increased or leveled off (Strode et al., 2015). The reasons for this trend are not fully understood and possible causes might be an increase in precursor emissions such as related to an increase in oil and gas exploration in the NFR, upward trends in background ozone and/or a shift in the chemical regime. Understanding the reasons behind these trends and how they relate to ozone production from local emissions is crucial for developing strategies aimed at the further reduction of ambient ozone levels.

Complex meteorology and flow patterns due to the high elevation and varied terrain and a mix of diverse pollution sources (e.g., urban emissions, strong point sources such as large power plants and industrial complexes and airports, and area sources such as agricultural emissions, emissions from oil and gas development, biogenic emissions, and wildfires) in the NFR pose challenges with respect to characterizing, modeling, and forecasting air quality and the underlying processes. In summer 2014, the State of Colorado and NSF Front Range Air Pollution and Photochemical Experiment (FRAPPÉ) and the fourth deployment of the NASA DISCOVER-AQ were carried out jointly to investigate the drivers of summertime ozone in the NFR (Pfister et al., 2017). A comprehensive set of chemical and meteorological measurements was collected from five aircraft, multiple mobile vans, ozonesondes, lidars, tethered balloons, and also at numerous operational and additional surface sites between 15 July and 20 August 2014 with most DISCOVER-AQ platforms ending on 10 August. The flight patterns of all aircraft and the full data set including data from surface sites are publicly available at http://www-air.larc.nasa.gov/missions/discover-aq/discover-aq.html website.

The field campaign data have been used in previous works to study the drivers behind NFR summertime ozone. Using different approaches these studies found that, in general, oil and gas production and mobile emissions contribute to high ozone levels with VOCs such as larger alkanes playing an important role (e.g., Mc. Duffie et al., 2016; NCAR/Atmospheric Chemistry Observations and Modeling (ACOM) Laboratory (2017); Evans & Helmig, 2017); the quantification and relevance of the different drivers vary depending on the study location, time periods and methods used. Schroeder et al. (2017) explored the validity of using satellite column ratios of formaldehyde (CH_2O) to nitrogen dioxide (NO_2) as an indicator of near-surface ozone sensitivity. They found that the ratios for the NFR that fall into the "ambiguous regime" span a larger range than for other regions in the United States and attribute this to nonhomogeneous vertical distributions of CH_2O and NO_2 in the lower troposphere and the fact that near-surface conditions may be decoupled from conditions at the top of the PBL and the lower free troposphere. Nearly half of the column ratios measured on board the NASA P-3 aircraft in the NFR fall in the range 0–2 (i.e., radical limited or in the transition/ambiguous regime), emphasizing the importance of VOCs to ozone production in the NFR. Background ozone also is considered a potential contributor to high NFR surface ozone. Kaser et al. (2017) focus on the diurnal cycle of entrainment by analyzing aircraft spirals conducted over six key surface sites. Entrainment through boundary layer growth was found to be most important in the early morning, adding up to ~5 ppbv/hr to surface ozone, but local chemical production dominates during the day. The entrained ozone can originate from long-range transport but might also be related to local ozone from the previous day that has been recycled as a result of mountain-valley recirculation. These complex and interrelated processes add to the challenge of source attribution studies but all point toward VOCs playing a significant role.

This study builds upon previous findings and characterizes the relevance of different VOCs to local ozone production in the NFR. Knowledge about the role of the different VOC precursors and tracing them back

to their source will provide valuable information to policy makers to address the NFR ozone problem. To achieve this objective, we use the regional Weather Research and Forecast Model with Chemistry (WRF-Chem) version 4. The authors contributed to this model version with the inclusion of an Integrated Reaction Rate (IRR) capability, similar to the capability included in the U.S. EPA Community Multiscale Air Quality model (CMAQ). The IRRs provide individual gas-phase reaction rates thus allowing to explore the details of the chemical transformations that are described in the model's chemical mechanism and to identify important chemical pathways and key chemical characteristics (Jang et al., 1995; Jeffries & Tonnesen, 1994).

In addition to the IRR, we added a number of other diagnostics to the WRF-Chem model: The output of trace gas tendencies, which represent the changes in a species concentration (e.g., ozone) before and after certain model processes such as chemistry or advection, is calculated in the model and the capability to calculate trajectories during runtime. This work is focused on a case study for 12 August 2014. On this day, a strong upslope event carried airmasses from the NFR to the nearby mountains that even "spilled" over the Continental Divide into the adjacent valleys on the Western Side of the Divide. The upslope event was sampled by the NSF/NCAR C-130 aircraft and surface ozone measurements at the mountain sites peaked at over 80 ppb in the late afternoon/evening (Pfister et al., 2017).

2. Model Setup and Field Campaign Data

In this section, we provide information on the model configuration, the emission inputs, and on the field campaign measurements that were used to evaluate the model output.

2.1. Model Setup

We use version 4.0 of the WRF-Chem model (Fast et al., 2006; Grell et al., 2005) with the recently released IRR capability. Our setup includes 2 domains with a 12 km × 12 km outer domain covering the larger western United States and a 4 km × 4 km inner domain covering Colorado (not shown). We selected the Model for Ozone and Related chemical Tracers (MOZART) gas phase chemical scheme as described in Knote et al. (2014). For this scheme, the gas phase chemistry is an update to the MOZART-4 chemistry (Emmons et al., 2010) by including a more detailed speciation of aromatics, updated isoprene chemistry, and N_2O_5 heterogeneous chemistry. Aerosol representation is based on the 4-bin Model for Simulating Aerosol Interactions and Chemistry (Zaveri et al., 2008). For chemical initial and lateral boundary conditions, we use global Real Time Air Quality Modeling System output (Sullivan et al., 2015). Our WRF-Chem simulations are started on 10 August 6 UTC and run until 13 August 6 UTC. We reinitialize the meteorology every 24 hr with reanalysis fields but keep the chemistry fields from the previous cycle. The results in this paper exclusively focus on model output for the inner domain and from the last initialization cycle.

We present results from six simulations, which allows us to test the robustness of our findings in light of some of the major uncertainties in air quality simulations. The uncertainty due to the anthropogenic emission input has been addressed with four simulations that all employ identical meteorology but different emission inventories. Two other simulations were conducted in which we kept anthropogenic emissions the same but changed the model physics so as to test the impact of different model meteorology and transport. We emphasize that the simulations we conducted for this study should not be considered as covering the full range of possible model uncertainties nor do we intend to represent a true ensemble or explore the sensitivity of the model to specific settings or determine one optimal configuration. Rather the purpose is to provide a more robust foundation for our conclusions by capturing some of the major underlying model uncertainties. A more detailed discussion on the effects of different model configurations in WRF-Chem simulations for FRAPPÉ is given in Abdi-Oskouei et al. (2018). Previous work by Gilliam et al. (2015) also provides an in-depth analysis of the impact of uncertainty in meteorology on air quality simulations with WRF-CMAQ over the contiguous United States.

For the set of emission sensitivity simulations, the meteorological driving fields are taken from 6-hourly ECMWF operational analysis fields available from NCAR's Research Data (https://rda.ucar.edu/). Weak analysis nudging in the outer domain only is applied for all cycles. The vertical extent of both domains stretches from the surface to 50 hPa with 51 vertical levels. The vertical resolution is not user defined through eta levels and the level thickness for the three lowermost levels is 56, 81, and 106 m. The setup

Table 1
Key Configurations Settings for the Set of WRF-Chem Simulations

	Emissions	Met.	Levels	PBL	Urb. Phy.	Nudging
EPA2014 (Base)	NEI 2014	ECMWF	51	YSU	yes	d01
NEI2011adj	Adj. NEI 2011	ECMWF	51	YSU	yes	d01
S05	See text	ECMWF	51	YSU	yes	d01
EPA2014_2xOG	NEI 2014 2x OG	ECMWF	51	YSU	yes	d01
EPA2014_phys	NEI 2014	ECMWF	37	MYNN	no	d01/d02
EPA2014_phys2	NEI 2014	ERA Interim	47	MYNN	yes	d01/d02

Note. Listed are emission inputs, driving meteorological fields, number of vertical levels, boundary layer scheme, and whether urban physics and grid nudging in the outer (d01) and/or inner (d02) domain were activated.

applies the following physics settings: YSU planetary boundary layer (PBL) scheme (Hong et al., 2006; Hong, 2010; Hu et al., 2013), the Monin-Obukhov similarity scheme (Janjic, 1994), the Noah land surface model (Tewari et al., 2004), the Rapid Radiative Transfer Model for GCMs (RRTMGs) radiation schemes (Iacono et al., 2008), the Grell-Devenyi ensemble cumulus scheme (Grell & Devenyi, 2002), Thompson microphysics (Thompson et al., 2008), a single layer urban physics scheme and land use categories based on the MODIS land-cover classification of the International Geosphere-Biosphere Programme and modified for the Noah land surface model.

Using this setup, we conducted four runs with different emissions inventories (Table 1). These are based on the best available information available at the time of the study for the region and period of interest. Since we do not allow for feedbacks between meteorology and chemistry, all the above simulations generate identical meteorology.

- *Simulation NEI2011_adj*. The anthropogenic emissions for this simulation are based on the U.S. EPA National Emission Inventory (NEI) version 2011 v2, which is available to WRF-Chem users at a 4-km spatial resolution. We were provided access to sector specific information for this inventory for five sectors (area sources, mobile sources, area oil and gas sources, point oil and gas sources, and nonoil point sources) (Stu McKeen, NOAA, personal communication). Based on previous literature (e.g., Anderson et al., 2014; Fujita et al., 2012; McDonald et al., 2012; NCAR/ACOM, 2017) as well as detailed evaluation of our model simulations (not discussed here) we applied the following updates to the base inventory: a reduction of mobile emissions by 50% of all species for both the outer and inner domains and a doubling of the oil and natural gas (O&G) sector emissions for the inner domain. For the latter we also applied the adjustments to all species except for ethane (C_2H_6) and propane (C_3H_8) for which we found reasonable agreement with the aircraft data using the base inventory (results for C_2H_6 are not shown here, but evaluation with aircraft C_3H_8 measurements are shown in section 2.3.1). A general underestimate in VOC emissions from the O&G sector in bottom-up inventories has also been found in previous work (e.g., Pétron et al., 2014).
- *Simulation S05*. This inventory is based on work described in detail in the final FRAPPÉ report to the State of Colorado (NCAR/ACOM, 2017). The underlying emissions generated with the Sparse Matrix Operator Kerner Emissions (SMOKEs) modeling system are based on a combination of U.S. EPA NEI 2017 projected emissions and actual 2014 activity data for oil and gas sources and electric generation units. To improve the base emissions, the study performed a comprehensive evaluation with aircraft and ground-based campaign data and from this suggested a factor of 2 increase in all mobile ethyne emissions, a doubling of mobile (onroad and off road) emissions in all species for the non-Denver urban and O&G region and doubling in O&G NO_x and VOC emissions aside from ethane.
- *Simulation EPA2014*. These emissions are based on SMOKE output provided by the U.S. EPA which include criteria pollutant and precursor emissions from the 2014 EPA platform (U.S. EPA, 2018a) as implemented for the National Air Toxics Assessment (U.S. EPA, 2018b). The area sources are available on a 12-km spatial resolution, with point sources on a per location basis. No adjustments were applied to this inventory.
- *Simulation EPA2014_2xOG*. For the fourth emission sensitivity simulation, we doubled the O&G emission in EPA 2014 emissions for all species except for higher alkanes (BIGALK), benzene, and toluene

Table 2
Emission Totals (in Metric Tons Species/Year) for the Entire Northern Front Range (NFR) From the Three Different Anthropogenic Emission Inventories as Well as the NEI EPA 2014 With Doubled Oil and Gas Emissions

	NFR (39.3–40.8 N, −105.35–−104 W)			
Species (mw)	NEI2011adj	EPA2014	S05	EPA2014_2xOG
CO (28)	41,749	72,996	61,907	74,946
NO (30)	6,846	7,085	7,037	8,043
NO_2 (46)	933	1,165	1,220	1,329
BIGALK (72)	20,118	9,548	14,137	18,920
C_2H_6 (30)	6,188	6,837	12,330	13,224
C_3H_8 (44)	5,249	3,846	9,535	7,512
BIGENE (56)	374	273	313	278
CH_3CHO (44)	105	134	91	147
C_3H_6 (42)	332	407	522	430
CH_2O (30)	291	224	180	314
CH_3OH (32)	156	246	267	254
ISOP (68)	3	6	22	6
APIN (136)	34	44	30	44

Note. BIGALK represents lumped alkanes for C > 3, BIGENE lumped alkenes for C > 3. The molecular weight (mw) for each species is specified.

for which we tripled the O&G emissions. This was motivated by a large low bias in comparison to aircraft data (section 2.2.1).

To account for uncertainties in meteorology and transport, we perform two additional simulations (Table 1) which are based on the EPA 2014 emissions but in which we changed the model physics and/or driving reanalysis fields, which leads to different meteorology and transport; that is, our full set of simulations covers three different meteorological conditions. For *EPA2014_phys* the main changes compared to the above runs are: 37 specified vertical eta levels (which leads to a level thickness of 12–16 m for the three lowermost altitudes), the use of the MYNN 2.5 level TKE boundary layer scheme (Janjic, 2001; Janjic, 2000), the Grell 3-D ensemble scheme for cumulus physics (Grell & Freitas, 2014). Additionally, we turned off urban physics and applied active grid nudging above the PBL in both domains. The main changes for *EPA2014_phys_2* compared to EPA2014_phys include 47 vertical levels without specified eta levels resulting in a thickness for the three lowest altitude levels of 46, 63, and 86 m, respectively, the use of the Morrison two-moment microphysics scheme, the use of ECMWF ERA-Interim reanalysis (available from NCAR's RDA) for meteorological initial and boundary conditions, and the activation of urban physics.

2.2. Comparison of Emission Inventories

A comparison of the total emission strength for the NFR (defined as ranging from 39.3 to 40.8 N and from 105.35 to 104 W) for the three different inventories as well as the EPA 2014 inventory with doubled O&G emissions is provided in Table 2. Figure S1 in the supporting information outlines the NFR region the total emission strength is calculated for and four other regions (OG, City, FHnorth, and FHsouth), which are used in the analysis later. Emission totals for the four separate regions are given in Table S1. For the latter we specify the values in units of average emission flux and not as domain total to account for the difference in area between the four regions (2,800, 2,544, 2,112, and 1,648 km^2 for OG, City, FHnorth, and FHsouth, respectively).

The Foothills regions (FHnorth and FHsouth) are located in the fairly pristine mountainous regions to the west of the NFR with little contribution of local anthropogenic emissions (Table S1). The OG and City regions reflect the areas where O&G and urban emissions dominate, respectively. O&G related tracers such as higher alkanes (BIGALK), propane (C_3H_8), and ethane (C_2H_6) are largest for the OG region, whereas more urban tracers such as NO_x, acetaldehyde (CH_3CHO) or higher alkenes (BIGENE) dominate in the City region. The different base inventories agree roughly in the total NO_x emissions, but especially large differences are seen for various VOC species such as higher alkanes, ethane, and propane, which mostly are related to the O&G sector. A doubling/tripling of O&G emissions in the EPA 2014 inventory brings emission totals for these VOC species closer in line with NEI 2011_adj and S05, that is, the inventories that are built upon an increase for O&G emissions from a base inventory but results in the highest NO_x emissions across all inventories (the O&G sector accounts for roughly ~10-20% of the overall NFR NO emissions in the different inventories).

Biogenic emissions were calculated online in WRF-Chem based on the Model of Emissions of Gases and Aerosols from Nature v2.04 (Guenther et al., 2012) option and emission totals as well as the average emission flux for 12 August 2014 are included in Table 3. Biogenic emissions are impacted by solar radiation and temperature and for this reason are identical among the simulations with different emission scenarios but differ for the simulations where we also changed the model physics. All simulations rely upon a 50% increase in the emission factors for biogenic monoterpenes and a 50% decrease in the emission factors for biogenic isoprene because our model evaluation revealed a low model bias for biogenic monoterpenes and a high model bias in biogenic isoprene (see section 2.3.1). A similar overestimate in the WRF-Chem estimated biogenic isoprene emissions has also been found by Bash et al. (2016) and Ryu et al. (2018).

Table 3
Emission Totals in (Metric Tons Species/Year) and (in Parenthesis) Average Emission Flux (g/km^2/hr) for Biogenic Isoprene (ISOP Bio) and Monoterpene (APIN Bio) Emissions

Species (mw)		OG	City	FHnorth	FHsouth	NFR
Base runs	ISOPbio (68)	2,622 (2,566)	4,973 (5,356)	4,013 (5,205)	3,740 (6,217)	28,539 (4,134)
	APINbio (136)	121 (119)	501 (540)	1,079 (1,340)	847 (1,409)	2,514 (3,64)
EPA2014_phys	ISOPbio (68)	2,653 (2,596)	5,250 (5,654)	4,140 (5,371)	3,875 (6,442)	29,491 (4,272)
	APINbio (136)	116 (113)	511 (551)	1,093 (1,418)	864 (1,437)	2,502 (362)
EPA2014_phys_2	ISOPbio (68)	2,822 (2,761)	5,344 (5,756)	4,508 (5,848)	4,072 (6,770)	30,506 (4,419)
	APINbio (136)	127 (124)	484 (521)	1,149 (1,490)	889 (1,478)	2,566 (372)

Note. Results are calculated from WRF-Chem online biogenic emissions for 12 August, and results are shown for individual regions as well as the entire Northern Front Range. The molecular weight (mw) for each species is specified.

As expected and evident from Tables 2 and 3, the total biogenic emissions for 12 August 2014 for isoprene and monoterpenes dominate over the anthropogenic source. Different model physics change the emission strengths by up to about ~10%. The largest total biogenic emissions of isoprene are estimated for the City due to an abundance of planted broadleaf trees in and around the urban area, but the average emission flux is highest for FHsouth. The contribution of monoterpenes is highest for the Foothills regions, where native needle leaf trees dominate. For fire emissions, we use the Fire Model from NCAR (FINN) v1.5 (Wiedinmyer et al., 2011), but these are expected to have little effect on the results given there had been no notable impact from fires during the considered time period.

2.3. Model Evaluation

2.3.1. Aircraft Measurements

We use measurements from the NSF/NCAR C130 for the flight on 12 August 2014 for evaluating the performance of the model in representing key trace gases. NO and NO_2 data have been collected with a two-channel chemiluminescence instrument (Weinheimer et al., 1994), ozone with a Chemiluminescence instrument (Ridley et al., 1992), formaldehyde (CH_2O), and ethane (C_2H_6) by infrared spectrometry (Richter et al., 2015) and VOCs by in situ gas chromatography mass spectrometry (Apel et al., 2015) as well as offline analysis of whole air canister samples by gas chromatography mass spectrometry (Colman et al., 2001). Acetaldehyde measurements have been conducted using the NCAR Proton Transfer Reaction-Quadrupole Mass Spectrometer (PTR-MS) (Karl et al., 2009).

The 20140812 flight was designed to measure the upslope flow of pollution from the NFR into the mountains and consisted of two parts. The first part (~12–16 LT) was targeted at characterizing daytime pollution and emissions in the Front Range, and the second part (~17–21 LT) followed the upslope transport from the NFR toward the Divide and into the adjacent valleys to the West (Pfister et al., 2017). A topographical map of the NFR and nearby mountains and the two different parts of the C-130 flight is provided in Figure S1.

Figure 1 compares time series of measured and modeled ozone, NO_x, and various VOCs. Figure 2 shows a comparison of the vertical profiles for ozone, NO_x, and BIGALK (lumped higher alkanes with C > 3) separately for the two different parts of the flight. The VOCs shown are selected based on their potential role in ozone chemistry as stated in previous literature (e.g., McDuffie et al., 2016) and also on discussions later in this study. For species where two different types of measurements are available, both data sets are shown. Evaluation statistics are listed in Table S2.

All model realizations show a similar behavior despite the differences in emissions and configuration. Ozone, overall, is biased low at all altitudes, except for EPA2014_phys_2, which, on average, agrees better with the observations but still misses some of the high peaks and from all simulations shows the largest underestimated variability. EPA2014_phys_2 is the simulation driven by different meteorological reanalysis fields and has the most difference in simulated meteorology and winds, which suggests that transport errors might explain a large part of the model biases. This is supported by comparing time series of measured and modeled winds along the flight paths (Figure S2) showing that all simulations are to some degree deficient in representing the measured winds, specifically during the first part of the flight. Part of the differences also arise from interpolating the hourly model output to the 1-min resolution of the aircraft data. Filtering the data set for when the modeled wind direction agrees with the observations to within a certain sector can

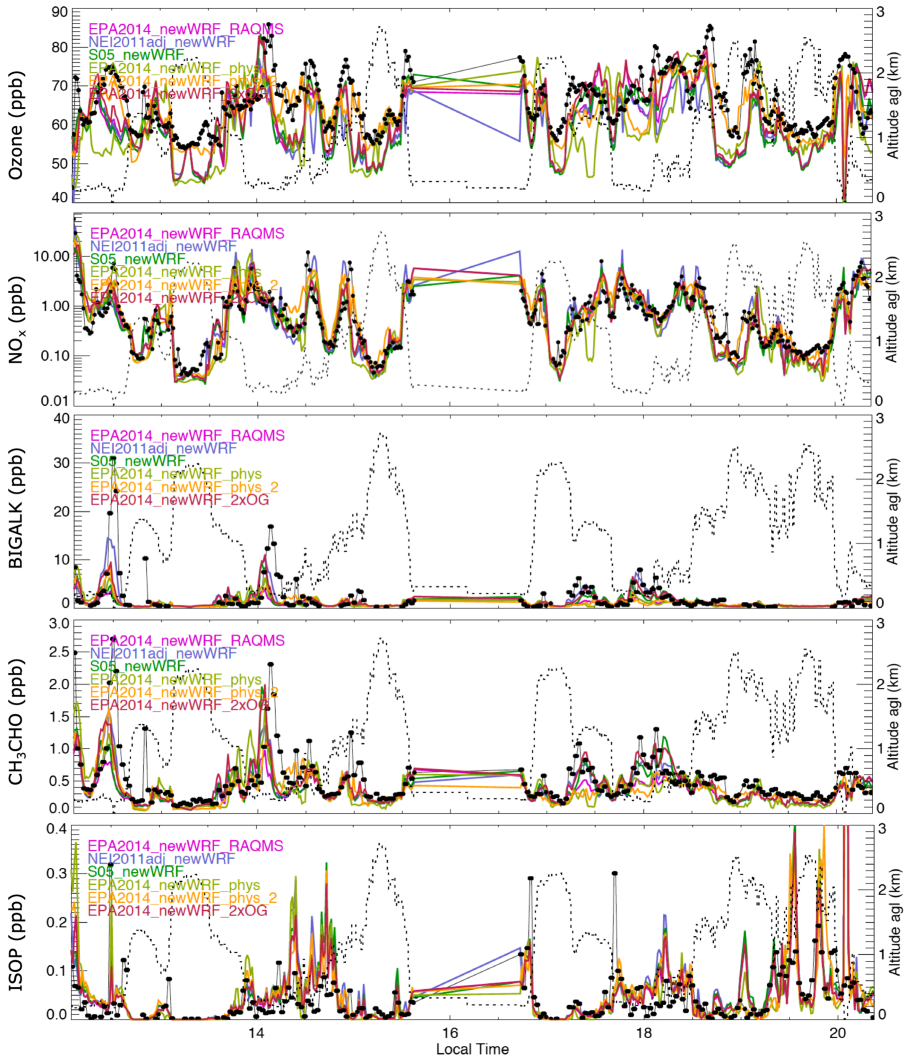

Figure 1. Time series of ozone, NO_x, formaldehyde, BIGALK, acetaldehyde (CH_3CHO), CH_2O and isoprene from measurements (black dots with TOGA measurements indicated by solid circles, WAS or PTR-MS measurements by diamond symbols), and the six different model simulations. Aircraft flight altitude above ground level is shown by the dotted line.

slightly improve the model agreement, specifically for directly emitted species, but also notably reduces the number of available data points. For example, filtering for an agreement in wind direction to within 30° reduces the number of data points by 25% and for three out of the six model runs reduces the RMSE by 4%–7% (for EPA2014_phys the RMSE increases by 3% and for two other simulations changes by <0.1%). Similarly, improvement is gained in a test case with higher temporal resolution output but the improvement is smaller than the range spanned by the different model realizations that is seen in Figures 1 and 2.

Modeled NO_x agrees fairly well, on average. The agreement across the different model runs is more variable during the first part of the flight whereas all models show a small low bias near the surface during the second part of the flight. BIGALK near the surface is underestimated significantly during the first part of the flight that was all flown within the NFR (i.e., close to source regions). From Figure 1, it is seen that the model is missing the high peaks in the measurements and this is in line with a large underestimate in the variability (Table S2). This is not unexpected as the model dilutes emissions by injecting them into a model grid that is larger than the actual plume and thus is not capturing the fresh and intense emission plumes that were intercepted by the aircraft.

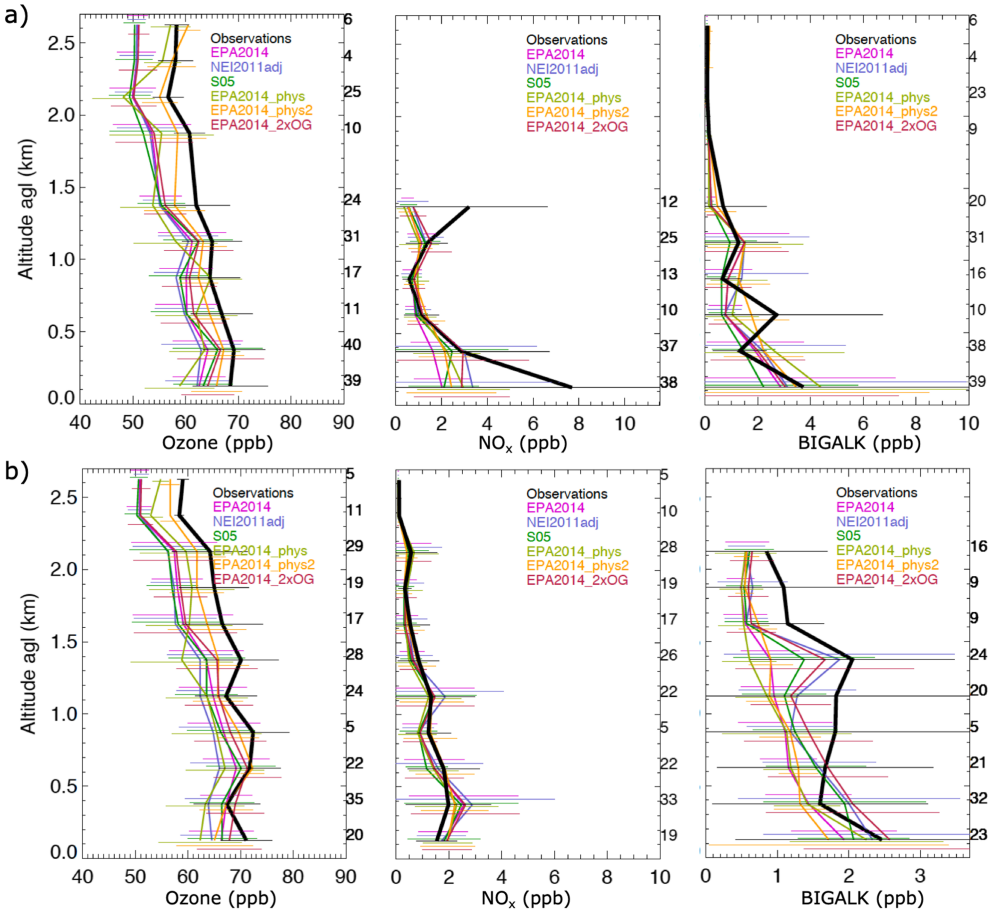

Figure 2. Vertical average over 25-km altitude bins (solid lines) and median (dotted lines) for (a) the first part and (b) the second (upslope) part of the 0812 C-130 flight. Only altitude bins with >3 data points are shown. Note that the scale for BIGALK changes between the different parts of the flight.

Similar results as for BIGALK are derived for acetaldehyde (CH_3CHO) (vertical profiles not shown). Formaldehyde (CH_2O) is captured well by all model simulations in terms of both magnitude and variability. Isoprene (ISOP), in contrast, is overestimated in all simulations despite a reduction in biogenic emissions. Due to the different spatial allocation of biogenic versus anthropogenic emissions, isoprene mixing ratios reach highest values for the Foothills legs in both measurements and simulations. Similarly, the model has a low bias for monoterpenes (not shown) despite the 50% increase in monoterpene emission factors in WRF-Chem.

To reduce the impact of transport errors in the comparison, we show in Figure 3 different modeled and measured trace gas relationships. The relationship of NO_x versus CO suggests that aside from NEI2011_adj, which has the lowest CO emissions (Table 2); all other inventories tend to overestimate the amount of CO emitted relative to NO_x. CO mostly comes from mobile emissions whereas NO_x in the NEI2011_adj comes from about 50% mobile, 40% area, and 10% O&G sources (roughly similar contributions for *EPA2014* and *S05*). The NO_x versus C_3H_8 relationship, with C_3H_8 used as an indicator for airmasses impacted by O&G sources, is fairly well represented by all model results suggesting a reasonable representation of modeled O&G sources of NO_x. The ratio of BIGALK versus C_3H_8 ranges across the different emission inventories with *NEI 2011_adj* most closely aligned with the observations suggesting that the NEI 2011_adj most closely resembles actual emissions ratios from the O&G emission sector.

In addition to ratios mostly relevant to assess emission ratios, we also show three other metrics to provide insight into the model's performance in representing ozone production. First, we show the ratio of CH_3CHO to CH_2O. Both species are produced from photochemical production and also have direct

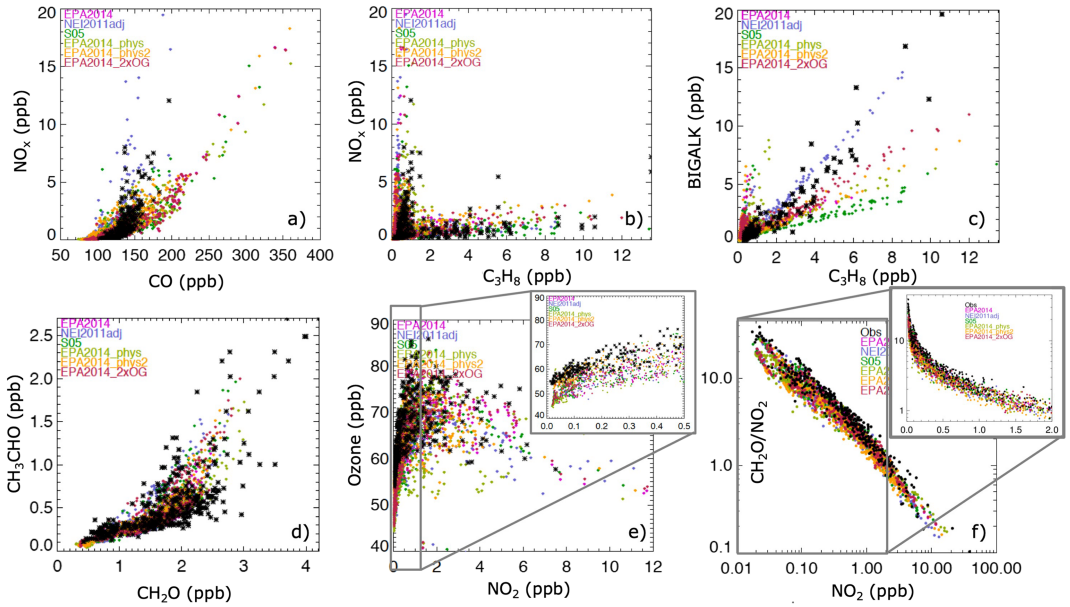

Figure 3. Measured (black) and modeled (colored) relationships for (a) NO_x to CO, (b) NO_x to propane (C_3H_8), (c) BIGALK to C_3H_8, (d) CH_3CHO to CH_2O, and (e) O_3 to NO_2 (with inlet showing a zoom into the low NO_2 concentration range). (f) The measured and modeled CH_2O/NO_2 ratio as function of NO_2 both plotted on a logarithmic scale (the inlet shows a zoom into the lower NO_2 range with NO_2 now on a linear scale). Results are shown for the 0812 C130 flight and for data points below 1.5 km.

emissions and, as will be shown later, play an important role in ozone production in the NFR. This ratio is well reflected in all simulations. Other metrics shown are the ratio of ozone versus NO_2 and the ratio of CH_2O to NO_2 as a function of NO_2 and also these are simulated well in the model.

Ozone mixing ratios sharply increase with increase in NO_2 from low to moderate values and then gradually decline with further increase in NO_2. Ozone mixing ratios at very low NO_x (or NO_2) levels can be taken as indicator for the background ozone (this term is used loosely here to define ozone coming into the NFR). For the measurements, the estimated ozone transported into the domain from outside (~55 ppb) is about 5–10 ppb higher compared to most simulations, except for EPA2014_phys_2. This is in line with the low bias in ozone mixing ratios at all altitudes discussed above and confirms that the most likely source for this low model bias is an underestimate in transported ozone and/or the lateral boundary conditions. The CH_2O/NO_2 ratio shown here as a function of NO_2 is frequently used to diagnose local photochemical regimes, with lower ratios indicating a radical-limited environment, and higher ratios indicating a NO_x-limited environment (e.g., Martin, 2004; Tonnesen & Dennis, 2000). These two regimes are separated by a "transition" environment where ozone is equally sensitive to radicals and NO_x. For Colorado, Schroeder et al. (2017) found a range of $0.9 < CH_2O/NO_2 < 1.8$ that lies in the transition/ambiguous region. Most data points for the 20140812 flight lie above this transition zone indicating that most aircraft measurements were conducted in a NO_x-limited environment. This does not suggest that the NFR is dominantly NO_x limited, since the aircraft flight data only provide a limited sampling. A large part of this flight was conducted in the more remote Foothills and also that aircraft samples were collected above ~300-m agl, hence not right near the emission sources and are not necessarily representative of surface conditions. Aircraft data were also only collected after 12 pm and therefore not representative of morning conditions. The ability of the model to represent these "photochemical metrics" despite differences in absolute metrics, however, does provide confidence in the model simulating the essential drivers behind ozone production in the NFR.

2.3.2. Surface Measurement

For evaluation of the model simulations in representing surface conditions, we use ozone and wind measurements at three surface sites: Longs Peak, a high altitude site in Rocky Mountain National Park (Benedict et al., 2018), Rocky Flats North, an operational monitoring site operated by the Colorado Department of Public Health and Environment and located in the NFR close to the Foothills, and the

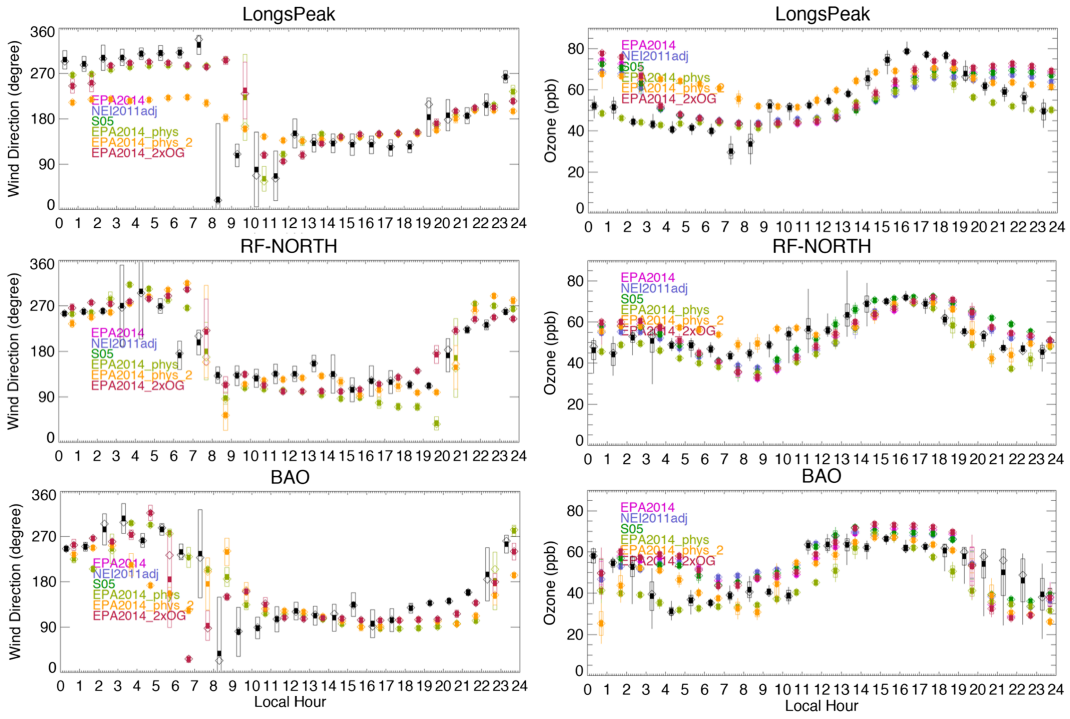

Figure 4. Comparison of modeled to measured surface winds (left) and ozone mixing ratios (right) at selected ground sites for 12 August 2014: Longs Peak (top), Rocky Flats North (middle), and BAO (bottom). Shown are hourly mean (filled symbols), median (open symbols), and standard deviation (bars). For ozone, the range spanned by the minima and maxima is also indicated by vertical bars. Measurements are in black, model results as indicated in the legend.

Boulder Atmospheric Observatory (BAO), operated by NOAA (McDuffie et al., 2016) and located to the northeast of the Denver metro area at the intersection of the regions dominated by urban and by O&G emissions. Figure S1 indicates the location for the three sites. Time series of surface wind direction and ozone mixing ratios at these three sites for 12 August 2014 are shown in Figure 4. Hourly statistics have been derived from 1-min measurements and from hourly instantaneous model results that have been linearly interpolated to the 1-min resolution of the observations (which explains the smaller variability in the model). We chose to interpolate the hourly model data to the 1-min resolution of the measurements so as to preserve the variability in the measurements, which, as can be seen from the graphs, can be significant over the course of 1 hr.

Overall, the model shows the measured wind patterns with downsloping winds switching to upslope flows in the morning and their reversal in the late afternoon/evening. The timing of the changes in wind direction, however, differ between the model and the observations and among the model simulations, which will have an impact on the transport and mixing of different emission sources. This transport error together with generally larger uncertainty in models simulating the growth of the planetary boundary layer lead to overall larger differences (~5–10 ppb) in early morning and evening surface ozone in the model, whereas midday ozone mixing ratios agree rather well for most model simulations at the NFR sites. At Longs Peak, the delay in the modeled onset of the upslope flows results in a delay in the late afternoon/evening ozone peak. Nighttime ozone at Longs Peak is significantly overestimated by up to ~15 ppb for most simulations except for *EPA2014_phys* which agrees well with the measurements. From all simulations, *EPA2014_phys* has the finest vertical resolution near the surface (section 2.1) and is the only simulation not applying urban physics, suggesting that model physical processes including winds and PBL contribute to these differences. As stated in Pfister et al. (2017), this site is also impacted by local circulation patterns which cannot be resolved by the model's grid resolution.

In addition, to these three surface sites, we include surface ozone data from all other surface monitoring sites available during the campaign in the evaluation. The temporal and spatial evolution of surface ozone from measurements and for EPA2014 is shown in Figure 5. In the early morning (9 LT), the highest surface ozone

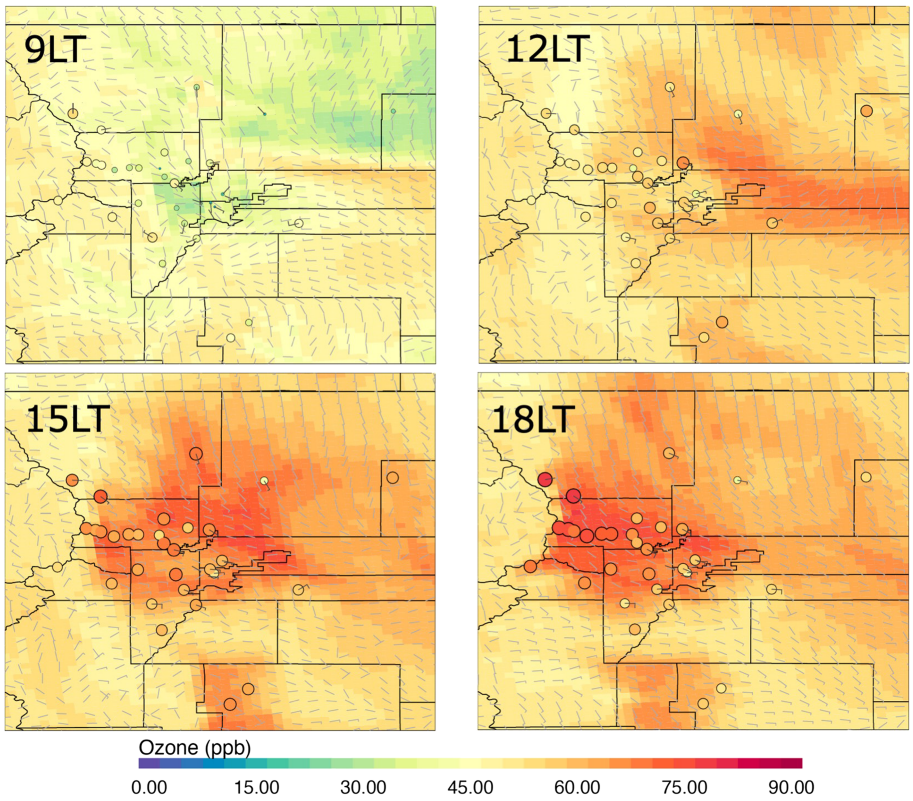

Figure 5. Maps of simulated surface ozone and winds for 12 August at 9, 12, 15, and 18 LT for *EPA2014*. Ozone and wind measurements at surface sites are added to the maps.

is seen at the high elevation areas to the West of the NFR and also over the Eastern plains, whereas the effects of nighttime ozone titration are still evident in the NFR. At noon, the spatial pattern reverses and local ozone production in the NFR leads to highest ozone mixing ratios in this region. East-southeasterly upslope transport of NFR ozone to the West is evident and becomes more pronounced during the afternoon. By 18 LT, the highest ozone mixing ratios are shown over the mountains with mixing ratios close to and even exceeding values in the NFR earlier in the day. The model overestimates the afternoon surface ozone mixing ratios in the NFR which likely is related to its delayed onset of and/or weaker upslope transport, but nevertheless, these graphs demonstrate that the model is proficient in simulating the measured spatial and temporal patterns. However, as also shown earlier, the simulations are affected by uncertainties in transport and localized effects. To demonstrate the impact of different model settings and inputs, we include in Figure S3 similar maps for 18 LT for all simulations. The shown maps reflect comparable overall behavior across all model simulations but the different model treatments lead to variations in the distribution and magnitude of the modeled surface ozone mixing ratios. No clear conclusion can be drawn about which of the model simulations shows the best performance in representing the field campaign measurements.

3. Results and Discussion

The evaluation results as well as the evaluation of the model and inputs in previous works provide confidence in applying the model for conducting a source contribution analysis. Here we discuss the analysis for four regions (Figure S1), which have been chosen based on emission characteristics: the greater Denver area (City), an area dominated by oil and natural gas production (OG), and two regions in the Foothills (a region North (FHnorth) and a region South (FHsouth)). The average composition within the boundary layer for 12 August 2018 within these regions is analyzed. We note that chemistry is not only

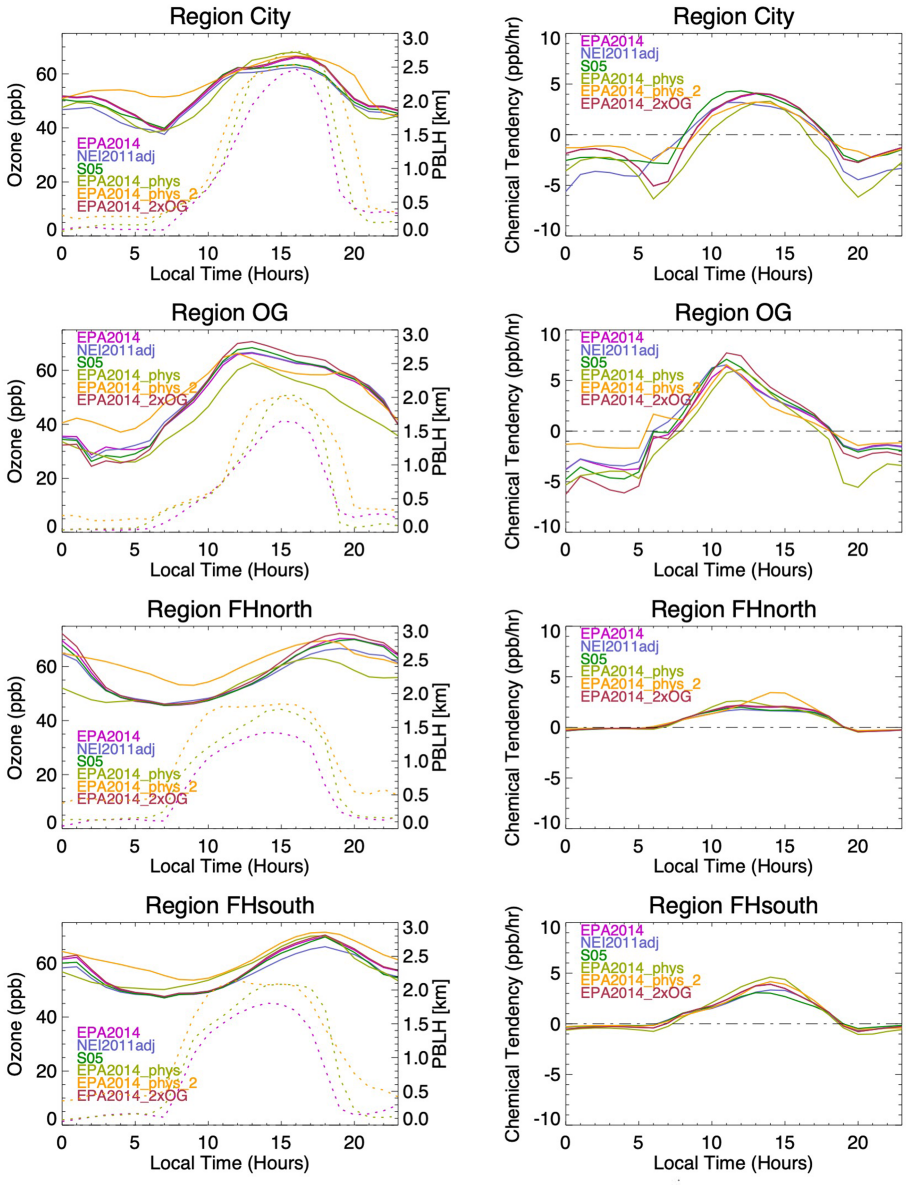

Figure 6. (left) Ozone mixing ratios (solid lines) and PBLH (dotted lines). (right) Chemical tendencies (net chemical ozone production, PO_3). Values shown are averaged within the PBL for the different model simulations. Results for four regions are shown (from top to bottom): City, OG, FHnorth, and FHsouth.

impacted by the emissions but also by airmass exchange between the regions, which is not addressed directly here.

3.1. Regional Surface Ozone Production

We begin by looking at the surface ozone mixing ratios and net photochemical ozone production (PO_3) for the four analysis regions and confined to the first model layer. The latter can be derived from both the model tendencies and the IRR output. The average diurnal cycle for these parameters as well as for the PBL height for 12 August 2014 is shown in Figure 6. The results from the different model simulations are similar, but the model scenarios with changed emissions are more closely aligned whereas the simulations with altered physics settings show a larger spread reflecting the strong influence of transport and meteorology.

Figure 6 shows clear differences in the diurnal cycle in both ozone mixing ratios and PO_3 between the four regions. The diurnal cycle for surface ozone mixing ratios possesses a sharper and higher peak for the OG

compared to the City region and peaks in the midafternoon for the City region compared to noontime for OG. This different behavior in OG can, to a large part, be explained by two factors playing together: First, OG has a slower growing PBL compared to City, which leads to the emitted pollutants being more concentrated. Second, as shown in Figure S4, for all simulations daytime NO_x is lower in OG compared to City (average daytime mixing ratios of ~3 ppb for City compared to ~1 ppb for OG in EPA2014), while the opposite is the case for VOCs (daytime mixing ratios of ~17 ppb compared to ~8 ppb for EPA2014). This is expected in light of the different emissions in these regions. As will be discussed in section 3.2, specifically, VOCs that strongly contribute to ozone formation are elevated in OG leading to higher OH reactivity and which in turn leads to efficient and rapid PO_3 (as discussed below). But because of the initially smaller NO_x mixing ratios in OG compared to City, efficient ozone production in OG cannot be sustained over the entire day while in City it will extend longer into the late afternoon. This is also supported by the analyses of NO_x in section 3.2.

The minimum ozone is reached in the early morning for City with the timing coinciding with rush hour, whereas OG has the minimum during nighttime. The rush hour ozone minimum in City is due to titration and is in line with a peak in NO_x mixing ratios that occurs because of a shallow PBL and at the same time high emission rate. The nighttime minimum in ozone mixing ratios in OG also coincides with the highest NO_x mixing ratios. The different behavior compared to City is likely due to a combination of factors including the fact that for most species, the O&G emissions have a less pronounced diurnal cycle, the pooling of urban emissions into the OG region during nighttime and early morning by drainage flows (Pfister et al., 2017) and a shallower nighttime PBL height in OG (Figure 6). At night, VOC mixing ratios in OG can reach close to 250 ppb (we cut off the scale for the graph to better visualize the daytime mixing ratios).

The Foothills regions, which are removed from local anthropogenic emissions, reflect mostly the characteristics of mountain sites with a reduced diurnal amplitude in ozone mixing ratios. These regions show a peak in ozone mixing ratios in the evening with the arrival of upslope transport from the NFR with FHnorth peaking later compared to FHsouth. Outside of the upslope related ozone enhancements, the mixing ratios represent background levels of ~50 ppb with higher mixing ratios for EPA2014_phys_2 in line with the analysis of the evaluation with aircraft data. NO_x and VOC mixing ratios are significantly reduced compared to the NFR regions and reflect a late afternoon/evening peak as a result of upslope transport from the NFR (Figure S4).

The diurnal cycles of net chemical ozone production show similar patterns as the ozone mixing ratios (Figure 6). City and OG exhibit a negative PO_3 during nighttime, early morning, and evening and positive net production during daylight hours. PO_3 reaches higher peaks for OG (~6–7 ppb/hr compared to 3–4 ppb/hr) yet the peak is broader for City. Integrating only daytime net PO_3 values (daytime is defined in here as the time period of positive net PO_3, ranging from 6–19 to 10–16 LT dependent on model run and region), we estimate a net total chemical ozone production in the range of 15–30 ppb for City and 30–40 ppb for OG for different model runs.

The Foothills regions exhibit small negative PO_3 values during nighttime and a broad positive PO_3 daytime peak with a total net PO_3 over the course of the day of ~15–20 ppb for FHnorth and ~20–25 ppb for FHsouth. This suggests that quite efficient ozone production continues to take place in these airmasses as they are transported into the mountains. We should note that the chemical tendencies in the standard version of the model are derived from hourly instantaneous values and that we restrict this analysis to the surface level only; as such it will not be fully representative of the integrated chemical production and loss. However, we calculated similar statistics using the hourly integrated IRR output averaged over the dynamic boundary layer and derived comparable results (not shown).

3.2. The Role of Different VOCs in Ozone Production

We now apply the IRR tool to examine the ozone chemical production in more detail. The IRR output for every grid cell and layer in the model is accumulated every time step of the model integration for all chemical reaction rates considered in the MOZART chemical mechanisms (Emmons et al., 2010; Knote et al., 2014). To obtain hourly values, we subtract the previous hour's IRR output from the current hour output and then average the mixing ratios within the PBL for the four regions. The PBL average rather than only the surface value is used to account for the fast mixing and airmass exchange within the PBL. The Python Environment for Reaction Mechanisms/Mathematics (PERMM) (Henderson et al., 2010; Henderson et al., 2011) was then

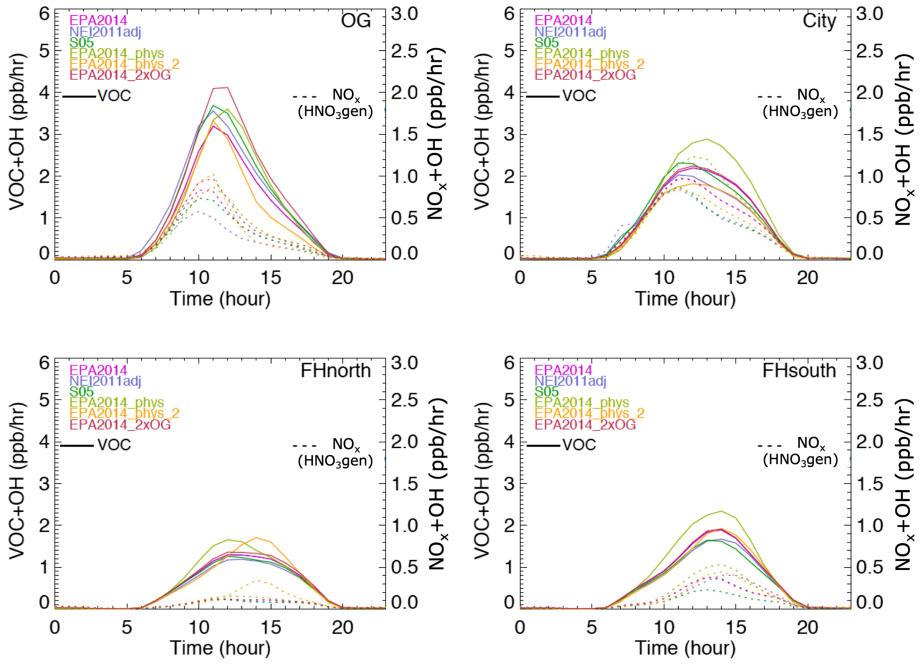

Figure 7. Diurnal cycle of the amount of VOCs (solid lines, primary ordinate) and NO_x (dotted lines, secondary ordinate) reacting with OH in (ppb/hr) for the different model realizations. Results for (from top left to bottom right): OG, City, FHnorth, and FHsouth.

used to postprocess the data. PERMM was used to isolate chemical process rates for selected grid cells allowing for tracking of plumes and the evolution of the PBL.

In a first step, we use the IRR to calculate the first order loss rate of different VOCs with hydroxyl radicals (OH), which provides a measure of an airmass to produce organic peroxy radicals and is one way to assess the roles of VOCs in the formation of surface ozone. A common way to assess this measure is by deriving the OH reactivity (OH loss frequency in s^{-1}). We use a similar metric but base our analysis on the amount of OH reacting with VOCs measured in (ppb/hr). For simplicity, we refer to this measure as "OH-VOC-IRR." Our definition of VOCs also includes methane and carbon monoxide (CO). Similar to VOCs, we also estimate the "NO_x reactivity," which is derived by calculating the generation of nitric acid (HNO_3) from IRR output. The "NO_x reactivity" includes all reactions to produce HNO_3, but the major pathway during daytime is through the reaction NO_2 + OH (92-99%).

Figure 7 depicts the diurnal cycles for OH-VOC-IRR and NO_x reactivity for the four different regions. The shapes of the diurnal cycles are similar to what was seen for PO_3 with (1) a more narrow and higher peak for the OG compared to the City region and (2) moderate broad peaks for the Foothills regions with FHsouth reaching higher values than FHnorth. OH reactivity for the VOCs reaches up to 4 ppb/hr for OG, 2–3 ppb/hr for the City region, and 1–2 ppb/hr for the Foothills regions. Integrating OH-VOC-IRR over 24 hr, we calculate the total amount of OH reacted as about 20 ppb for OG, 18 ppb for the City, 11 ppb for the FHnorth, and 14 ppb for the FHsouth region for EPA2014. Different model scenarios can result in relatively pronounced differences in total OH-VOC-IRR even though the general regional patterns remain the same. Doubling O&G emissions, for example, increases OH-VOC-IRR from 20 to 26 ppb for the OG region with little changes to the other regions (which suggests that overall transport between the different regions had a small impact) or changing the model physics can vary daily OH-VOC-IRR from 15 to 22 ppb in the City region (which demonstrates the influence of local small-scale dynamics on chemistry).

NO_x reactivity plays the largest role in the City region where it is about 2–3 times smaller than the daily integrated OH-VOC-IRR. For the OG, FHsouth, and FHnorth regions, we estimate that the NO_x reactivity is about 3–6 times, 5–8 times, and 6–10 times smaller compared to OH-VOC-IRR, respectively. The relative

Table 4
Process Analysis Table for NO_x 8- to 18-LT-Integrated Production and Loss

	OG	City	FHnorth	FHsouth
NO - > NO_2	53.6	53.9	23.4	33.4
NO + HO_2	33.3	36.1	14.3	21.8
NO + RO_2	20.3	17.8	9.1	11.6
NO_2 + $h\nu$ - > NO + O	40.5	23.7	22.3	30.6

Note. Columns show the different regions and rows show the different chemical processes. Absolute predicted values (ppb) are listed.

ratio of OH-VOC-IRR and NO_x reactivity gives insight into the preference for OH to react with either VOC or NO_x thus indicating whether a region tends to be more VOC or NO_x limited. Our results suggest that the City region is closer to being VOC limited whereas OG and the Foothills regions are closer to being NO_x limited regime. These results are in line with the regional differences in NO_x and VOC emissions (Table S1) and mixing ratios (Figure S4).

Process analysis also allows us to gain insight into the roles of different pathways in which NO leads to ozone production. In Table 4, we list the different pathways for the photochemically active part of the day (8–18 LT). Both reactions NO + HO_2 and NO + RO_2 lead to ozone production. For City, the higher NO emissions result in the largest NO + HO_2 reactions (36.1 ppb) of the four regions. For OG, higher VOC emissions increase the abundance of peroxyl radicals (RO_2), resulting in this region having the largest reaction NO + RO_2 (20.3 ppb). Ultimately, the produced NO_2 can be photolyzed and lead to ozone formation. OG has the highest values for the 8- to 18-LT integrated NO_2 photolysis (40.5 ppb), which is in line with our findings earlier for OG having the highest net $P(O_3)$.

For policy making, it is not only the total VOC reactivity (or in our case denoted as OH-VOC-IRR) that is of interest but understanding which VOCs play the dominant role in local ozone production as this can provide information on the role of individual emission sectors and help inform emission control strategies. Each VOC has widely differing reaction rates and shows differing potential to form ozone, but this information is generally not easily derived from measurements or models. With the IRR capability, this information can be calculated during postprocessing of the output. Figure 8 shows the results of this analysis and, similar to before, illustrates the OH-VOC-IRR diurnal cycle for the four regions, but now, we only show results for EPA2014 and separate the total OH-VOC-IRR by contributions from different VOCs. Only the six most relevant VOC species are highlighted.

In all regions, CO represents the largest single contribution to OH-VOC-IRR, which emphasizes the role of CO in determining the oxidation capacity of the atmosphere. CO mixing ratios show similar diurnal cycles and regional differences as NO_x mixing ratios with higher daytime values in the City versus OG region (~150 ppb compared to ~110 ppb; not shown).

Formaldehyde (CH_2O) is the next most important VOC species in all study regions. CO and CH_2O together account for roughly half of the total OH-VOC-IRR in each region. This agrees with previous studies (e.g., Lee et al., 1998 or Mathur et al., 2005) who also found a high contribution of CO and CH_2O to OH reactivity in the United States. In the OG region, the other major players are BIGALK and acetaldehyde (CH_3CHO) with each about 10% followed by isoprene and propane. For the City region, other major VOC species are isoprene (ISOP), CH_3CHO, and BIGALK accounting for about 8%, 7%, and 6%, respectively. Our findings are in line with the recent study by Chen et al. (2019) who attributed a large part of the OH reactivity over the United States during summertime to CH_2O and CH_3CHO.

In the Foothills regions, the role of ISOP increases in relative importance accounting for about 17% and 14% in FHnorth and FHsouth, respectively. This reflects the increased role of biogenic emissions to ozone production over the pristine mountainous terrain. We still see nonnegligible contributions from NFR related emission tracers such as BIGALK or CH_3CHO; albeit, the latter is also produced during chemical production. Other VOCs contribute smaller amounts but combined still make up a notable contribution in each region.

To explain the pathways through which CO and CH_2O contribute to ozone production, we quantify in Table 5 the 8- to 18-LT integrated HO_2 production and loss for the four different regions. The fraction of HO_2 generated from the reaction CO + OH is ~24.6%–29.8% of total production. City has the highest CO emission from the four regions considered (Table S1) and the contribution to HO_2 via the CO + OH pathway is about 11.7 ppb (29.8%). The second major source of HO_2 is from CH_2O (20.7%–23.6%), including the photolysis of CH_2O (~40%) and the reaction CH_2O + OH (~60%). The absolute contribution to HO_2 through CH_2O is highest for the OG region (8.7 ppb) in line with the highest VOC emissions and mixing ratios for this

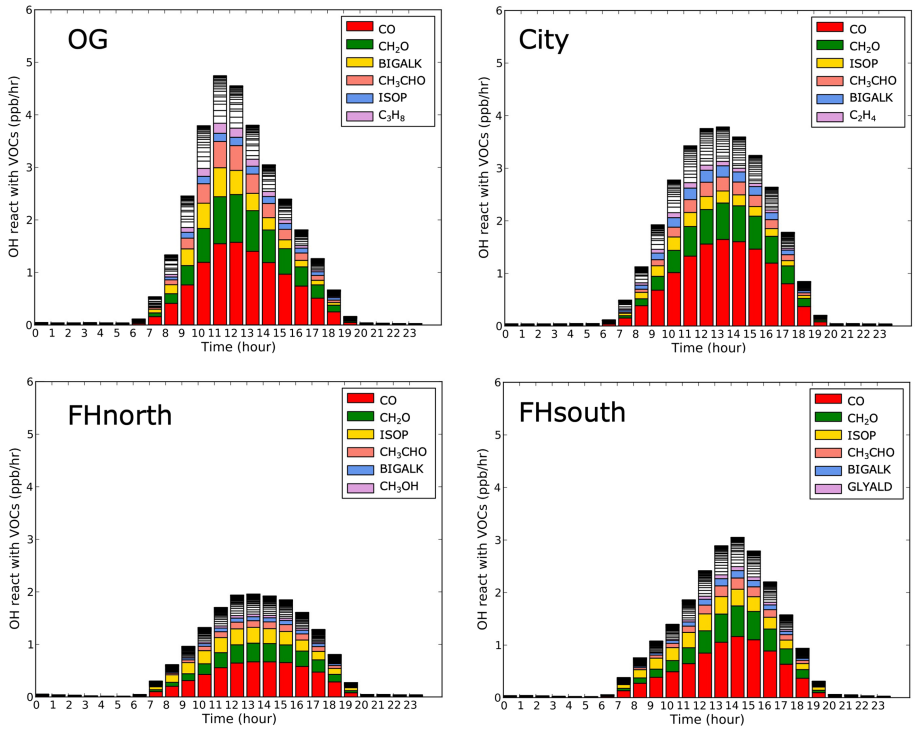

Figure 8. Diurnal cycle of OH-VOC-IRR (amount of VOCs reacting with OH in (ppb/hr)). The six VOCs with the highest daily average contribution to each scenario are marked in color; unfilled boxes represent other VOCs which together amount to total OH-VOC-IRR. Results are shown for *EPA2014*. Results for (from top left to bottom right): OG, City, FHnorth, and FHsouth.

region. Together these two reactions account for about half of the total HO_2 generation in all regions. The major loss reaction for HO_2 is the reaction with NO to produce OH and NO_2 (66.4%–89.3%), which is the dominant reaction in the NFR that leads to ozone production (Table 4 and discussion above).

The six sensitivity simulations, while varying from each other somewhat, agree in the general ranking of the VOCs. Figure S5 illustrates the daily total OH-VOC-IRR for different species and the set of model scenarios. Notable outliers are the dominance of BIGALK in the OG region for NEI2011_adj and EPA2014_2xOG. Both these simulations have the largest emissions for BIGALK in the OG region (Table S1). For the Foothills regions, EPA2014_phys shows an overall higher contribution from ISOP compared to other simulations, which likely is linked high biogenic emissions (Table 3) and differences in the diurnal cycle when compared to the other simulations (not shown here).

Table 5
Process Analysis Table for HO_2 8- to 18-LT Daily Production and Loss

	OG	City	FHnorth	FHsouth
Total HO_2 generation	39.8	39.2	21.1	27.3
HO_2 from CO + OH	10.3 (25.9%)	11.7 (29.8%)	5.2 (24.6%)	7.5 (27.4%)
HO_2 from CH_2O	8.7 (22.0%)	8.1 (20.7%)	5.0 (23.6%)	6.1 (22.3%)
Total HO_2 transfer to OH	40.8	40.4	21.5	27.9
HO_2 + NO ➔ OH + NO_2	33.3 (81.6%)	36.1 (89.3%)	14.3 (66.4%)	21.8 (78.2%)

Note. Columns show the different regions and rows show the different chemical processes. Absolute predicted values (ppb) are listed as well as the percentages (in parenthesis), that is, the contribution of a specific process to the total formation or termination process.

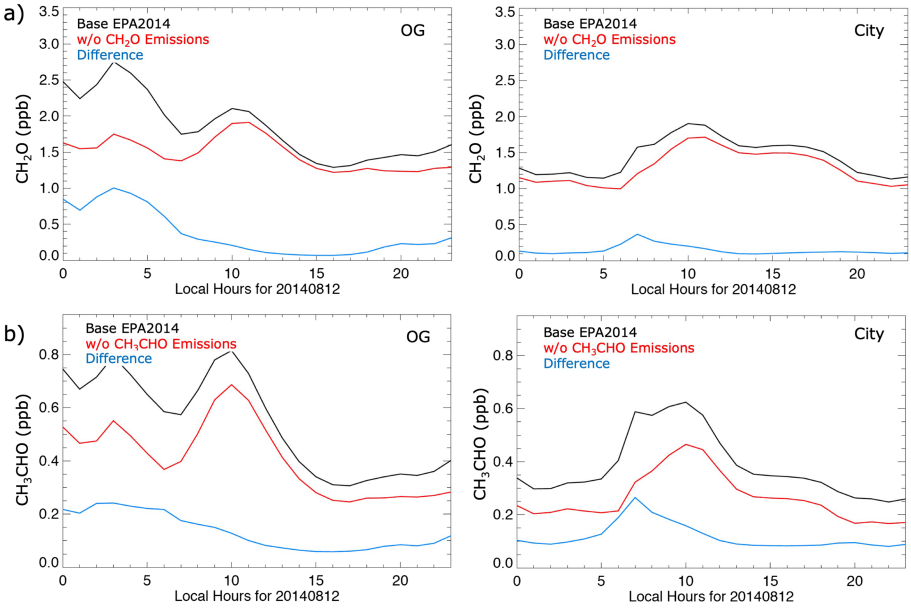

Figure 9. PBL average absolute mixing ratios for formaldehyde (a) and acetaldehyde (b) and their differences when between the base simulation and a simulation without direct emissions of either species in *EPA2014*. Results are shown for the OG (left) and City (right) regions.

3.3. Source Analysis for CO, Formaldehyde, and Acetaldehyde

The PERMM results show the dominance of CO, formaldehyde, higher alkanes, acetaldehyde, and isoprene to ozone formation in the FR and mountain areas to the West. CO mostly is controlled by background conditions as well as local emissions. Higher alkanes and isoprene can be related directly to local emissions, with isoprene mostly from biogenic sources and higher alkanes to the most part originating from sources related to oil and gas extraction and processing. Formaldehyde and acetaldehyde, however, have both direct emissions as well as chemical production in the atmosphere from precursor emissions and in order to provide valuable insight for developing emission control strategies, the amount of these trace gases needs to be traced back to a direct emission source. This brings up three questions: (1) Can we quantify the contribution of local CO emissions versus CO background concentrations to local ozone production; (2) what is the relative contribution of direct emissions of acetaldehyde and formaldehyde to ozone production in the NFR; and (3) what are the precursor species that lead to photochemically produced acetaldehyde and formaldehyde?

To address the first question, we conducted an additional sensitivity simulation based on the EPA2014 setup but in which we turned off all anthropogenic CO emissions within Colorado. In Figure S6, we include the resulting changes in CO and ozone mixing ratios for the four regions. Without CO emissions, the CO mixing ratios approach about 90–100 ppb and the largest reduction is found in City (>150 ppb). The resulting differences in ozone mixing ratios can reach up to ~1 and 1.4 ppb in OG and City, respectively. The highest impact is found for the Foothills regions (up to ~2 ppb). For all regions, the time of the maximum change in ozone aligns with the peak in ozone (Figure 6). The higher impact in the Foothills regions can be explained in that CO has a long lifetime (approximately weeks), thus experiences little chemical loss during the transport into the Foothills contrary to many of the reactive VOC species which lifetime is in the order of hours and less. These results, albeit for a case study only, suggest that the biggest benefit of local CO emission reductions could be expected in downwind regions.

To address the second question and estimate the relative contribution from direct emissions to atmospheric concentrations of acetaldehyde and formaldehyde, we conduct two additional simulations also based on EPA2014 in which we turn off anthropogenic emissions of formaldehyde and acetaldehyde, respectively. Formaldehyde mostly originates from various industrial, mobile and also O&G sources, whereas the dominant source of acetaldehyde is the mobile sector. The resulting change in formaldehyde and acetaldehyde mixing ratios is shown in Figures 9 and S7. We note that turning off acetaldehyde emissions will also

Table 6
Precursor Emission Species Leading to CH_2O Production

	OG	City	FHnorth	FHsouth
CH_4	**29.4%**	**26.7%**	**27.1%**	**25.6%**
CH_3OH	5.7%	4.4%	5.3%	5.2%
C_2H_4	3.8%	3.5%	2.7%	2.8%
C_2H_6	3.2%	0.3%	0.7%	0.0%
C_2H_5OH	1.2%	1.8%	1.3%	1.5%
C_3H_6	**7.9%**	**11.0%**	4.5%	4.7%
C_3H_8	2.4%	0.1%	0.1%	0.0%
BIGALK	**16.8%**	9.6%	**8.4%**	**8.2%**
BIGENE	4.1%	5.4%	3.2%	2.7%
ISOP	**7.9%**	**13.4%**	**26.2%**	**24.4%**
XYLENES	0.4%	1.5%	0.0%	0.0%
TOLUENE	0.0%	0.5%	0.0%	0.0%
TERP	0.4%	1.6%	6.2%	5.2%
Total	**83.2%**	**79.8%**	**85.9%**	**80.4%**

Note. Results for *EPA2014* are shown. The three highest contributions are highlighted in bold.

affect CH_2O mixing ratios and vice versa as discussed in more detail below. Turning off the direct emissions for either species changes ozone mixing ratios by less than 0.5 ppb.

Direct emissions of formaldehyde show the largest effect on CH_2O mixing ratios in the OG region during nighttime while in the City region we see the most impact in the early morning when a shallow boundary later leads to the accumulation of emissions (Figure 9). Overall, the contribution of direct emissions to CH_2O mixing ratios is relatively small and even less outside the NFR (Figure S7). For acetaldehyde, we find similar results except here direct emissions appear to have a higher impact compared to their role to CH_2O mixing ratios, specifically in the City region. For both species, however, we see that photochemical production is a major player which raises the question which precursor emissions contribute to the chemical production of these species.

PERMM was applied to find the emission composition of these secondary VOC species in order to answer the third question. First, all reactions that generate the target secondary VOC and the reactant VOCs are identified by PERMM. Then, the reactant species determined in the first step are applied as the products and PERMM is used to identify their reactants. These chain processes are continually executed until the reactant can be related to an emission species. Finally, the emission species are aggregated and their total contribution is calculated. An example for the chain for formaldehyde production for the OG region is shown in Figure S8, but due to the wealth of information, only parts of the different contributions are decipherable in the graphs. For clarity, we sum up all contributions that can be linked to species with direct emissions and summarize the results for the four regions for CH_2O and CH_3CHO production in Tables 6 and 7, respectively. We include results for EPA2014 only, but similar results are also derived for the other model scenarios.

Roughly one third of the photochemically produced formaldehyde is traced back to methane in both the OG and City regions through methylperoxy radicals (CH_3O_2) (Table 6). Other production chains that can be linked to species that relate to direct emissions to the most part include BIGALK (~17% for OG and 10% in City), ISOP (8% for OG and 13% for City), propene (C_3H_6) (8% for OG and 11% for City). and smaller contributions from methanol (CH_3OH), higher alkenes (BIGENE), ethene (C_2H_4), and C_2H_6. The contribution related to BIGALK also includes the pathway through acetaldehyde via production of acetylperoxy radicals (CH_3CO_3).

For the Foothills regions, the production of formaldehyde, which in absolute terms is less than for the NFR regions (~7-9 ppb versus 12–13 ppb) also shows the largest contribution from methane (~25%) with about the same amount attributable to isoprene, which together with the larger role of monoterpenes reflects the increased role of biogenic emissions. NFR tracers, however, also have notable contributions specifically from higher alkanes, ethanol, propene, and higher alkenes.

Table 7
Precursor Emission Species Leading to CH_3CHO Production

	OG	City	FHnorth	FHsouth
C_2H_6	**16.6%**	1.8%	6.2%	2.6%
C_2H_5OH	5.7%	12.1%	9.9%	**12.7%**
C_3H_6	**13.6%**	**26.2%**	**15.4%**	**16.3%**
C_3H_8	6.8%	0.6%	2.1%	0.8%
BIGALK	**43.7%**	**32.6%**	**40.7%**	**41.7%**
BIGENE	9.7%	**17.6%**	**14.4%**	12.3%
Total	**96.0%**	**91.0%**	**88.7%**	**86.4%**

Note. Results for *EPA2014* are shown. The three highest contributions are highlighted in bold.

Acetaldehyde production is mostly related to higher alkanes (44% in OG and 33% in City) either directly through $ALKO_2$ or through the production of MEK (Table 7). In the OG region, other major contributors are direct emissions of C_2H_6 and C_3H_6 (17% and 14%, respectively). Aside from BIGALK, the City region shows major contributions from C_3H_6 (26%), BIGENE (18%), and ethanol (C_2H_5OH) (12%). Higher alkanes also are the dominant precursor species in the Foothills regions followed by propene, higher alkenes, and ethanol.

Methane is also a relevant player in local ozone production given that methane is the largest source of formaldehyde and formaldehyde is the second largest contributor to HO_2 radicals (21-23%) (section 3.3)

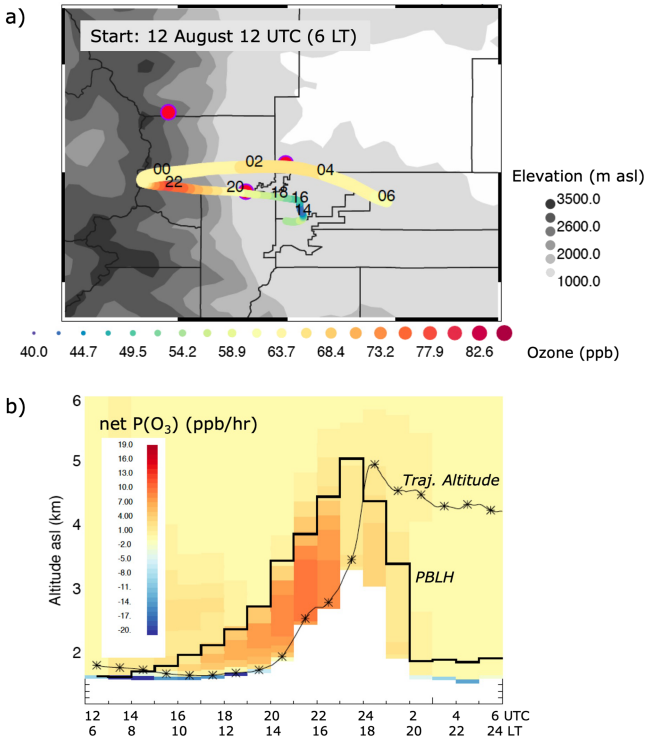

Figure 10. (a) Ozone (ppb) along a trajectory released in downtown Denver at 12 UTC (6 LT) with time (UTC) indicated. The three surface sites from Figure 1 are shown for orientation. (b) Time-altitude cross section of net chemical ozone production (ppb/hr) along the trajectory. Boundary layer height (thick boxed line) and trajectory altitude (thin line with symbols) are overlaid. Results from *EPA2014*.

with 67%–91% of the HO_2 involved in the NO to NO_2 reaction. To assess whether local methane emissions could play an important role, we conducted another sensitivity simulation. Typically, in WRF-Chem methane concentrations are constrained by climatology not considering direct emissions. To estimate the addition of local methane emissions, we increased the mixing ratios over the NFR and Foothills by adding 500- to 1,890-ppb background. The applied enhancement is in line with methane measurements over Platteville from the NASA P-3 aircraft during DISCOVER-AQ (not shown).

The resulting changes in surface ozone mixing ratios shown in Figure S6b are about 1 ppb or less in all regions and similar to what was seen before for the CO sensitivity test, largest in the Foothills regions. While this sensitivity test might represent an upper limit since, we increase methane across a larger region without allowing it to be transported out and the changes in ozone mixing ratios are fairly small; it does demonstrate that methane emissions might not only be of relevance on climate time scales but could also play a role when looking at short-term air pollution.

3.4. VOC Analysis Along an Airmass Trajectory

The diagnostic value of the IRR capability is further assessed in the analysis of the chemical evolution of an airmass during transport. For this, we make use of a capability of WRF which allows us to calculate forward trajectories during runtime from predefined locations and times and output meteorological and chemical parameters along the trajectory. While this method allows the release of multiple trajectories, we focus here only on a detailed discussion of one selected case, a trajectory that was released at ~200-m agl in downtown Denver on 12 August at 12 UTC (6 LT). Figure 10 shows ozone mixing ratios along the trajectory path as well as the net chemical ozone production, trajectory altitude and PBL height along the path. Other trace gases are shown in Figure 11a.

The trajectory started above the PBL but was entrained down to the surface after a couple hours. Around 16 UTC (10 LT), upslope winds develop with the trajectory turning westward and slowly moving toward the mountains. At 20 UTC (14 LT), the trajectory has traveled out of the urban area and reached the Foothills. About 4 hr later (~24 UTC or 18 LT), it reached the Continental Divide where it was lofted out of the PBL.

Initial ozone mixing ratios are about 55 ppb dropping by ~15 ppb when the trajectory enters the PBL (Figure 10) and is fueled by high NO_x (up to 25 ppb). Coinciding with the spike in NO_x, we see an increase in BIGALK related to colocated emission sources in the urban area (Figure 11). The chemical ozone production (Figure 10b) shows the prevalence of a net chemical loss near the surface as a result of the high NO_x mixing ratios. As the day progresses, photochemistry accelerates and the PBL rises. The trajectory travels toward the Foothills and on its path is fueled with local emissions of NO_x and VOCs such that the net chemical ozone production increases throughout the boundary layer. Maximum $P(O_3)$ values along the trajectory of 10 ppb/hr and peak ozone mixing ratios of ~80 ppb are reached at ~21 UTC (15 LT) at which time the trajectory has already traveled into the pristine mountain areas. As the trajectory travels into the mountains transporting all the pollutants with it, we see a decline in NO_x and BIGALK mixing ratios while at the same time isoprene from biogenic sources increases (Figure 11a). CH_2O mixing ratios remain enhanced during the entire photochemically active period. Ozone mixing ratios drop to ~60 ppb after the trajectory is lofted into the free troposphere and mixes with background ozone (westerly winds in the free troposphere result in reversal of transport direction).

Similar to before, we use the IRR diagnostics to assess the relevance of different VOC species to ozone production along the trajectory (Figure 11b). CO accounts for a large part of the total reactivity at all hours, but

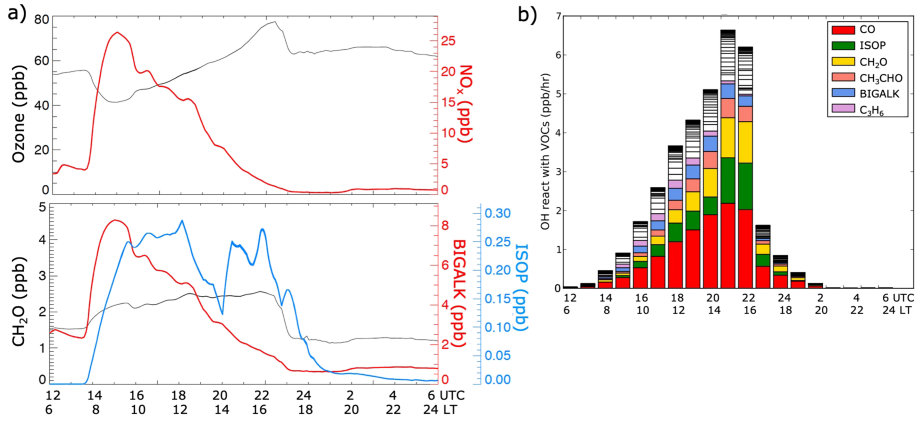

Figure 11. (a) Ozone, NO_x, CH_2O, BIGALK, and ISOPR along the trajectory shown in Figure 10. (b) OH-VOC-IRR (ppb/hr) along the same trajectory for the six VOCs that have the highest contribution. Results from *EPA2014*.

compared to the regional analysis discussed earlier, isoprene gains in importance with nearly equal contributions as CH_2O. CH_3CHO and BIGALK still have nonnegligible contributions to OH-VOC-IRR in the mountains, again reflecting the lasting impact of NFR emissions to photochemical ozone production in the pristine environment. OH-NO_x reactivity (not shown here) is about half of OH-VOC-IRR while the trajectory remains in the NFR but quickly drops during transport into the mountains.

3.5. Uncertainties and Limitations

We do acknowledge that the contribution made by any individual VOC to photochemical ozone formation might depend on environmental conditions and the mixing and chemical processing of different air masses will vary from day to day. Here we present the analysis of a single day case study; however, the conditions on the considered day represent typical patterns that are prevalent on high ozone days in the NFR and as such it is legitimate to assume that the presented results also roughly represent conditions that prevail on other high ozone days in the NFR.

While we consider uncertainties related to different emission inventories in this study, neither of the considered inventories account for emissions of sources that in recent studies have been identified as potentially making essential contributions to VOC emissions. These include the recent study by McDonald et al. (2018) who found that emissions from chemicals in pesticides, coatings, printing inks, adhesives, cleaning agents, and personal care products might constitute a larger source of VOCs than previously thought. Another study by Wang et al. (2019) determined terpene emissions from cannabis suggesting that cannabis growing operations in the NFR could be a source of highly reactive biogenic VOCs. Future studies are needed to estimate the potential impacts of these additional sources on summertime ozone in the NFR and relate their impact to emission sources conventionally included in emission inventories. Other sources of uncertainty such as the representation of deposition processes or the simplification of the chemical mechanisms as needed for implementation in 3-D models might add additional uncertainties to the simulation results but are not expected to significantly alter the conclusions.

4. Summary

The presented study examines the role of different VOCs to ozone production in the NFR and nearby mountains. For this we use the WRF-Chem model and a newly introduced diagnostics tool—the IRR. The IRR provides valuable diagnostics that can be used to explain a model simulation in terms of the budgets of, for example, radical initiation, propagation, and termination, production and loss of odd oxygen and ozone.

A set of model simulations is conducted to account for uncertainties in model emissions and physical parameterizations. We focus on a case study of 12 August 2014. This day was characterized by elevated ozone concentrations and upslope winds during daytime, which are typical conditions prevailing on high pollution days. The simulations are evaluated with field campaign data from the NSF/NCAR and State of Colorado FRAPPÉ and the NASA DISCOVER-AQ experiments that took place in Colorado in summer 2014 and

provided a comprehensive set of chemical and meteorological data. While the model has a number of shortcomings in representing measured mixing ratios, the set of different simulations and integration of different measurements and evaluation metrics demonstrates that the model is capable of representing the essential chemical drivers behind ozone production in the NFR.

Our analysis reveals that CO, formaldehyde, higher alkanes, acetaldehyde, and isoprene are among the VOC species that have the highest contribution to ozone production in the NFR. Of these, higher alkanes and isoprene are mostly related to direct emissions from oil and natural gas extraction and processing and to direct emissions from biogenic sources, respectively. Sensitivity simulations show that for formaldehyde and acetaldehyde the dominant fraction of their ambient mixing ratios in the NFR, however, is due to chemical production and not from direct emissions. Using the IRR tool, we can trace back the chemical-produced fraction to precursor species and emissions. Our results identify methane oxidation and emissions of higher alkanes, isoprene, ethane, and propane as the main contributors to the photochemical production of formaldehyde and acetaldehyde. While the exact ranking and quantification vary with changes in model inputs and configurations, the general conclusions are robust across the set of sensitivity simulations conducted. The combination of different model diagnostics also lets us assess the continued ozone production of an airmass originating in the NFR and being transported into the pristine mountain areas. We also note that CO and methane do play a key role in ozone production albeit they are often neglected in air quality analysis. Local emissions of CO and methane contribute up to ~2 and ~1 ppb to local ozone mixing ratios, respectively, with the largest effect in the nearby mountain areas.

Knowledge about the role of the different VOC precursors and tracing them back to their source and characterizing ozone production during airmass transport can provide valuable information to policy makers and can help develop more efficient, accurate, and cost-effective control strategies for meeting the ozone air quality standards. Our study is limited to a case study for a single day and while conditions of this day are typical for high ozone days, we acknowledge that they are not necessarily representing conditions for all high ozone days. This study also does not consider the effects of potentially important emission sectors such as personal care products or cannabis growing operations, that have been identified in recent studies as potentially important contributors to ozone pollution.

Acknowledgments
We acknowledge Alison Eyth and Barron H. Henderson at the U.S. Environmental Protection Agency for making SMOKE outputs for the NEI 2014 available and Brad Pierce at NOAA/NESDIS for providing output from the Real Time Air Quality Modeling System for use as chemical initial and boundary conditions. We thank Stuart McKeen at NOAA/ESRL who provided the Environmental Protection Agency NEI 2011v2 data. We acknowledge the highly valuable input provided by two anonymous reviewers. The observational data for this paper is publicly available at the FRAPPÉ/DISCOVER-AQ data archive (http://www-air.larc.nasa.gov/missions/discover-aq/discover-aq.html). The authors would like to thank the State of Colorado/Colorado Department of Public Health and Environment and the NSF for funding of FRAPPÉ and NASA for funding of DISCOVER-AQ. The authors acknowledge the use of WRF-Chem version 4.0 (http://www2.mmm.ucar.edu/wrf/users/download/get_source.html) and of NCAR ACOM WRF-Chem preprocessing tools (https://www2.acom.ucar.edu/wrf-chem). NCAR TOGA VOC measurements were carried out by Eric Apel (NCAR/ACOM). Aircraft VOC WAS samples have been collected and analyzed by Don Blake (UC Irvine). Dirk Richter, Peter Weibring, and James Walega (INSTAAR) contributed to collecting ethane measurements on the NCAR/NSF C-130, and Andy Weinheimer, Deedee Monzka, and Teresa Campos (NCAR/ACOM) are acknowledged for NSF/NCAR C-130 NO_x and ozone measurements. Lisa Kaser (now University of Innsbruck) is acknowledged for C-130 PTR-MS measurements. The National Center for Atmospheric Research is sponsored by the National Science Foundation.

References

Abdi-Oskouei, M., Pfister, G., Flocke, F., Sobhani, N., Saide, P., Fried, A., et al. (2018). Impacts of physical parameterization on prediction of ethane concentrations for oil and gas emissions in WRF-Chem. *Atmospheric Chemistry and Physics*, *18*, 16,863–16,883. https://doi.org/10.5194/acp-18-16863-2018

Anderson, D., Loughner, C., Diskin, G., Weinheimer, A., Canty, T., Salawitch, R., et al. (2014). Measured and modeled CO and NOy in DISCOVER-AQ: An evaluation of emissions and chemistry over the eastern US. *Atmospheric Environment*, *96*, 78–87. https://doi.org/10.1016/j.atmosenv.2014.07.004

Apel, E. C., Hornbrook, R. S., Hills, A. J., Blake, N. J., Barth, M. C., Weinheimer, A., et al. (2015). Upper tropospheric ozone production from lightning NO_x-impacted convection: Smoke ingestion case study from the DC3 campaign. *Journal of Geophysical Research: Atmospheres*, *120*, 2505–2523. https://doi.org/10.1002/2014JD022121

Bash, J. O., Baker, K. R., & Beaver, M. R. (2016). Evaluation of improved land use and canopy representation in BEIS v3.61 with biogenic VOC measurements in California. *Geoscientific Model Development*, *9*, 2191–2207. https://doi.org/10.5194/gmd-9-2191-2016

Benedict, K. B., Prenni, A. J., Sullivan, A. P., Evanoski-Cole, A. R., Fischer, E. V., Callahan, S., et al. (2018). Impact of Front Range sources on reactive nitrogen concentrations and deposition in Rocky Mountain National Park. *PeerJ*, *6*, e4759. http://doi.org/10.7717/peerj.4759

Chameides, W. L., Fehsenfeld, F., Rodgers, M. O., Cardelino, C., Martinez, J., Parrish, D., et al. (1992). Ozone precursor relationships in the ambient atmosphere. *Journal of Geophysical Research*, *97*(D5), 6037–6055. https://doi.org/10.1029/91JD03014

Chen, X., Millet, D. B., Singh, H. B., Wisthaler, A., Apel, E. C., Atlas, E. L., et al. (2019). On the sources and sinks of atmospheric VOCs: An integrated analysis of recent aircraft campaigns over North America. *Atmospheric Chemistry and Physics Discussions*, *19*(14), 9097–9123. https://doi.org/10.5194/acp-2019-115

Colman, J. J., Swanson, A. L., Meinardi, S., Sive, B. C., Blake, D. R., and Rowland, F. S. (2001). Description of the analysis of a wide range of volatile organic compounds in whole air samples collected during PEM-Tropics A and B. *Analytical Chemistry*, *73*, 3723– 3731, https://doi.org/10.1021/ac010027g

Colorado Department of Public Health and the Environment (2016). 2015 Air quality data report. Denver, Colorado: Colorado Department of Public Health and the Environment. APCD-TS-B1.

Cooper, O. R., Parrish, D. D., Ziemke, J., Balashov, N. V., Cupeiro, M., Galbally, I. E., et al. (2014). Global distribution and trends of tropospheric ozone: An observation-based review. *Elem Sci Anth*, *2*, 000029. http://doi.org/10.12952/journal.elementa.000029

Emmons, L. K., Walters, S., Hess, P. G., Lamarque, J.-F., Pfister, G. G., & Fillmore, et al. (2010). Description and evaluation of the Model for Ozone and Related chemical Tracers, version 4 (MOZART-4). *Geoscientific Model Development*, *3*, 43–67. https://doi.org/10.5194/gmd-3-43-2010

Evans, J. M., & Helmig, D. (2017). Investigation of the influence of transport from oil and natural gas regions on elevated ozone levels in the northern Colorado front range. *Journal of the Air & Waste Management Association*, *67*(2), 196–211. https://doi.org/10.1080/10962247.2016.1226989

Fast, J. D., Gustafson, W. I. Jr., Easter, R. C., Zaveri, R. A., Barnard, J. C., Chapman, E. G., & Grell, G. A. (2006). Evolution of ozone, particulates, and aerosol direct forcing in an urban area using a new fully-coupled meteorology, chemistry, and aerosol model. *Journal of Geophysical Research*, *111*, D21305. https://doi.org/10.1029/2005JD006721

Fujita, E. M., Campbell, D. E., Zielinska, B., Chow, J. C., Lindhjem, C. E., DenBleyker, A., et al. (2012). Comparison of the MOVES2010a, MOBILE6.2, and EMFAC2007 mobile source emission models with on-road traffic tunnel and remote sensing measurements. *Journal of the Air & Waste Management Association*, *62*(10), 1134–1149. https://doi.org/10.1080/10962247.2012.699016

Gilliam, R. C., Hogrefe, C., Godowitch, J. M., Napelenok, S., Mathur, R., & Rao, S. T. (2015). Impact of inherent meteorology uncertainty on air quality model predictions. *Journal of Geophysical Research: Atmospheres*, *120*, 12,259–12,280. https://doi.org/10.1002/2015JD023674

Grell, G., & Devenyi, D. (2002). A generalized approach to parameterizing convection combining ensemble and data assimilation techniques. *Geophysical Research Letters*, *29*(14), 505. https://doi.org/10.1002/jgrd.50823

Grell, G. A., & Freitas, S. R. (2014). A scale and aerosol aware stochastic convective parameterization for weather and air quality modeling. *Atmospheric Chemistry and Physics*, *14*, 5233–5250. https://doi.org/10.5194/acp-14-5233-2014

Grell, G. A., Peckham, S. E., Schmitz, R., McKeen, S. A., Frost, G., Skamarock, W. C., & Eder, B. (2005). Fully coupled "online" chemistry in the WRF model. *Atmospheric Environment*, *39*, 6957–6976.

Guenther, A. B., Jiang, X., Heald, C. L., Sakulyanontvittaya, T., Duhl, T., Emmons, L. K., & Wang, X. (2012). The Model of Emissions of Gases and Aerosols from Nature version 2.1 (MEGAN2.1): an extended and updated framework for modeling biogenic emissions. *Geoscientific Model Development*, *5*, 1471–1492. https://doi.org/10.5194/gmd-5-1471-2012

Henderson, B. H., Kimura, Y., McDonald-Buller, E., Allen, D. T., & Vizuete, W. (2011). Comparison of Lagrangian Process Analysis Tools for Eulerian Air Quality Models. *Atmospheric Environment*, *45*(29), 5200–5211.

Henderson B.H., Vizuete W., Jeffries H., &, Kim B. (2010). The influence of model resolution on industrial releases and ozone formation. *Journal of the Air and Waste Management Association*, Vol. *60*(9), 1105-1117.

Hong, S. Y. (2010). A new stable boundary layer mixing scheme and its impact on the simulated East Asian summer monsoon. *Quart. J. Roy. Meteor. Soc.*, *136*(651), 1481–1496. https://doi.org/10.1002/Qj.665

Hong, S. Y., Noh, Y., & Dudhia, J. (2006). A new vertical diffusion package with an explicit treatment of entrainment processes. *Monthly Weather Review*, *134*, 2318–2341. https://doi.org/10.1175/MWR3199.1

Hu, X.-M., Klein, P. M., & Xue, M. (2013). Evaluation of the updated YSU planetary boundary layer scheme within WRF for wind resource and air quality assessments. *Journal of Geophysical Research: Atmospheres*, *118*, 10,490–10,505. https://doi.org/10.1002/jgrd.50823

Iacono, M. J., Delamere, J. S., Mlawer, E. J., Shephard, M. W., Clough, S. A., & Collins, W. D. (2008). Radiative forcing by long-lived greenhouse gases: Calculations with the AER radiative transfer models. *Journal of Geophysical Research*, *113*, D13103.

Jang, J.-C. C., Jeffries, H. E., & Tonnesen, S. (1995). Sensitivity of ozone to model grid resolution – II. *Detailed process analysis for ozone chemistry. Atmos. Environ.*, *29*, 3101–3114.

Janjic, Z. (2000). Comments on "Development and evaluation of a convection scheme for use in climate models". *Journal of the Atmospheric Sciences*, *57*, 3686–3686.

Janjic, Z. (2001). Nonsingular implementation of the Mellor-Yamada Level 2.5 Scheme in the NCEP Meso model, Natl. Centers Environ. Predict., US Department of Commerce, National Oceanic and Atmospheric Administration, National Weather Service Camp Spring, MD, 1–61.

Jeffries, H. E., & Tonnesen, S. (1994). A comparison of two photochemical reaction mechanisms using mass balance and process analysis. *Atmospheric Environment*, *28*, 2991–3003.

Karl, T., Apel, E. C., Hodzic, A., Riemer, D. D., Blake, D. R., & Wiedinmyer, C. (2009). Emissions of volatile organic compounds inferred from airborne flux measurements over a megacity. *Atmospheric Chemistry and Physics*, *9*, 271–285. https://doi.org/10.5194/acp-9-271-2009

Kaser, L., Patton, E. G., Pfister, G. G., Weinheimer, A. J., Montzka, D. D., Flocke, F., et al. (2017). The effect of entrainment through atmospheric boundary layer growth on observed and modeled surface ozone in the Colorado Front Range. *Journal of Geophysical Research: Atmospheres*, *122*, 6075–6093. https://doi.org/10.1002/2016JD026245

Knote, C., Hodzic, A., Jimenez, J. L., Volkamer, R., Orlando, J. J., Baidar, S., et al. (2014). Simulation of semi-explicit mechanisms of SOA formation from glyoxal in aerosol in a 3-D model. *Atmospheric Chemistry and Physics*, *14*, 6213–6239. https://doi.org/10.5194/acp-14-6213-2014

Lee, Y.-N., Zhou, X., Kleinman, L. I., Nunnermacker, L. J., Springston, S. R., Daum, P. H., et al. (1998). Atmospheric chemistry and distribution of formaldehyde and several multioxygenated carbonyl compounds during the 1995 Nashville/Middle Tennessee Ozone Study. *Journal of Geophysical Research*, *103*(D17), 22,449–22,462. https://doi.org/10.1029/98JD01251

Martin, R. V. (2004). Space-based diagnosis of surface ozone sensitivity to anthropogenic emissions. *Geophysical Research Letters*, *31*, L06120. https://doi.org/10.1029/2004GL019416

Mathur, R., Shankar, U., Hanna, A. F., Odman, M. T., McHenry, J. N., Coats, C. J. Jr., et al. (2005). Multiscale Air Quality Simulation Platform (MAQSIP): Initial applications and performance for tropospheric ozone and particulate matter. *Journal of Geophysical Research*, *110*(D13), D13308. https://doi.org/10.1029/2004JD004918

McDonald, B. C., Dallmann, T. R., Martin, E. W., & Harley, R. A. (2012). Long-term trends in nitrogen oxide emissions from motor vehicles at national, state, and air basin scales. *Journal of Geophysical Research*, *117*, D00V18. https://doi-org.cuucar.idm.oclc.org/10.1029/2012JD018304

McDonald, B. C., de Gouw, J. A., Gilman, J. B., Jathar, S. H., Akherati, A., Cappa, C. D., et al. (2018). Volatile chemical products emerging as largest petrochemical source of urban organic emissions. *Science*, *359*(6377), 760–764. https://doi.org/10.1126/science.aaq0524

McDuffie, E. E., Edwards, P. M., Gilman, J. B., Lerner, B. M., Dube, W. P., Trainer, M., et al. (2016). Influence of oil and gas emissions on summertime ozone in the Colorado Northern Front Range. *Journal of Geophysical Research: Atmospheres*, *121*, 1–19. https://doi-org.cuucar.idm.oclc.org/10.1002/2016JD025265

NCAR/ACOM 2017: Pfister, Flocke, Lee and Schroeder, https://www.colorado.gov/airquality/tech_doc_repository.aspx?action = open&-file = FRAPPE-NCAR_Final_Report_July2017.pdf

Pétron, G., Karion, A., Sweeney, C., Miller, B. R., Montzka, S. A., Frost, G. J., et al. (2014). A new look at methane and nonmethane hydrocarbon emissions from oil and natural gas operations in the Colorado Denver-Julesburg Basin. *Journal of Geophysical Research: Atmospheres*, *119*, 6836–6852. https://doi.org/10.1002/2013JD021272

Pfister, G. G., Reddy, P. J., Barth, M. C., Flocke, F. F., Fried, A., Herndon, S. C., et al. (2017). Using observations and source-specific model tracers to characterize pollutant transport during FRAPPÉ and DISCOVER-AQ. *Journal of Geophysical Research: Atmospheres*, *122*, 10,510–10,538. https://doi.org/10.1002/2017JD027257

Richter, D., Weibring, P., Walega, J. G., Fried, A., Spuler, S. M., & Taubman, M. S. (2015). Compact highly sensitive multi-species airborne mid-IR spectrometer. *Applied Physics B: Lasers and Optics*, *119*(1), 119–131. https://doi.org/10.1007/s00340-015-6038-8

Ridley, B. A., Grahek, F. E., & Walega, J. G. (1992). A small, high-sensitivity, medium- response ozone detector suitable for measurements from light aircraft. *Journal of Atmospheric and Oceanic Technology*, *9*, 142–148.

Ryu, Y.-H., Hodzic, A., Barre, J., Descombes, G., & Minnis, P. (2018). Quantifying errors in surface ozone predictions associated with clouds over the CONUS: A WRF-Chem modeling study using satellite cloud retrievals. *Atmospheric Chemistry and Physics*, *18*, 7509–7525. https://doi.org/10.5194/acp-18-7509-2018

Schroeder, J. R., Crawford, J. H., Fried, A., Walega, J., Weinheimer, A., Wisthaler, A., et al. (2017). New insights into the column CH_2O/NO_2 ratio as an indicator of near-surface ozone sensitivity. *Journal of Geophysical Research: Atmospheres*, *122*, 8885–8907. https://doi.org/10.1002/2017JD026781

Simon, H., Reff, A., Wells, B., Xing, J., & Frank, N. (2015). Ozone trends across the United States over a period of decreasing NO_x and VOC emissions. *Environmental Science & Technology*, *49*(1), 186–195. https://doi.org/10.1021/es504514z

Strode, S. A., Rodriguez, J. M., Logan, J. A., Cooper, O. R., Witte, J. C., Lamsal, L. N., et al. (2015). Trends and variability in surface ozone over the United States. *Journal of Geophysical Research: Atmospheres*, *120*, 9020–9042. https://doi.org/10.1002/2014JD022784

Sullivan, J. T., McGee, T. J., Thompson, A. M., Pierce, R. B., Sumnicht, G. K., Twigg, L. W., et al. (2015). Characterizing the lifetime and occurrence of stratospheric-tropospheric exchange events in the rocky mountain region using high-resolution ozone measurements. *Journal of Geophysical Research: Atmospheres*, *120*, 12,410–12,424. https://doi.org/10.1002/2015JD023877

Tewari, M., F. Chen, W. Wang, J. Dudhia, M. A. LeMone, K. Mitchell, et al. (2004). Implementation and verification of the unified NOAH land surface model in the WRF model. *20th conference on weather analysis and forecasting/16th conference on numerical* weather prediction, pp. 11–15.

Thompson, G., Field, P. R., Rasmussen, R. M., & Hall, W. D. (2008). Explicit forecasts of winter precipitation using an improved bulk microphysics scheme. Part II: Implementation of a new snow parameterization. *Monthly Weather Review*, *136*(12), 5095–5115.

Tonnesen, G. S., & Dennis, R. L. (2000). Analysis of radical propagation efficiency to assess ozone sensitivity to hydrocarbons and NO_x 2. Long-lived species as indicators of ozone concentration sensitivity. *Journal of Geophysical Research*, *105*(D7), 9227–9241. https://doi.org/10.1029/1999JD900372

US EPA (2018a). *Preparation of Emissions Inventories for the Version 7.1 2014 Emissions Modeling Platform for the National Air Toxics Assessment (Technical Support Document)*. North Carolina: U.S. Environmental Protection Agency, Research Triangle Park. https://www.epa.gov/air-emissions-modeling/2014-version-71-platform

US EPA (2018b). *EPA's 2014 National Air Toxics Assessment (Technical Support Document)*. North Carolina: U.S. Environmental Protection Agency, Research Triangle Park. https://www.epa.gov/national-air-toxics-assessment/2014-nata-technical-support-document

Wang, C.-T., Wiedinmyer, C., Ashworth, K., Harley, P. C., Ortega, J., & Vizuete, W. (2019). Leaf enclosure measurements for determining volatile organic compound emission capacity from Cannabis spp. *Atmospheric Environment*, *199*, 80–87. https://doi.org/10.1016/j.atmosenv.2018.10.049

Weinheimer, A. J., Walega, J. G., Ridley, B. A., Gary, B. L., Blake, D. R., Blake, N. J., et al. (1994). Meridional distributions of NO_x, NO_y, and other species in the lower stratosphere and upper troposphere during AASE II. *Geophysical Research Letters*, *21*, 2583–2586. https://doi.org/10.1029/94GL01897

Wiedinmyer, C., Akagi, S. K., Yokelson, R. J., Emmons, L. K., Al-Saadi, J. A., Orlando, J. J., & Soja, A. J. (2011). The Fire INventory from NCAR (FINN): A high resolution global model to estimate the emissions from open burning. *Geoscientific Model Development*, *4*, 625–641. https://doi.org/10.5194/gmd-4-625-2011

Zaveri, R., Easter, R., Fast, J., & Jerome, L. P. (2008). Model for Simulating Aerosol Interactions and Chemistry (MOSAIC). *Journal of Geophysical Research*, *113*. https://doi.org/10.1029/2007JD008782